MNRAS **454,** 1432–1452 (2015) doi:10.1093/mnras/stv2053

CFHTLenS: weak lensing constraints on the ellipticity of galaxy-scale matter haloes and the galaxy-halo misalignment

Tim Schrabback,[1,2,3⋆] Stefan Hilbert,[4,5] Henk Hoekstra,[3] Patrick Simon,[1] Edo van Uitert,[1,6] Thomas Erben,[1] Catherine Heymans,[7] Hendrik Hildebrandt,[1] Thomas D. Kitching,[8] Yannick Mellier,[9,10] Lance Miller,[11] Ludovic Van Waerbeke,[12] Philip Bett,[1] Jean Coupon,[13] Liping Fu,[14] Michael J. Hudson,[15,16] Benjamin Joachimi,[6] Martin Kilbinger[9,10] and Konrad Kuijken[3]

[1]*Argelander Institute for Astronomy, University of Bonn, Auf dem Hügel 71, D-53121 Bonn, Germany*
[2]*Kavli Institute for Particle Astrophysics and Cosmology, Stanford University, 382 Via Pueblo Mall, Stanford, CA 94305-4060, USA*
[3]*Leiden Observatory, Leiden University, Niels Bohrweg 2, NL-2333 CA Leiden, the Netherlands*
[4]*Excellence Cluster Universe, Boltzmannstr. 2, D-85748 Garching, Germany*
[5]*Ludwig-Maximilians-Universität, Universitäts-Sternwarte, Scheinerstr. 1, D-81679 München, Germany*
[6]*Department of Physics and Astronomy, University College London, Gower Street, London WC1E 6BT, UK*
[7]*The Scottish Universities Physics Alliance, Institute for Astronomy, University of Edinburgh, Blackford Hill, Edinburgh EH9 3HJ, UK*
[8]*Mullard Space Science Laboratory, University College London, Holmbury St Mary, Dorking, Surrey RH5 6NT, UK*
[9]*Institut d'Astrophysique de Paris, UMR7095 CNRS, Université Pierre and Marie Curie, 98 bis boulevard Arago, F-75014 Paris, France*
[10]*Laboratoire AIM, CEA/Irfu/SAp Saclay, F-91191 Gif-sur-Yvette, France*
[11]*Department of Physics, Oxford University, Keble Road, Oxford OX1 3RH, UK*
[12]*Department of Physics and Astronomy, University of British Columbia, 6224 Agricultural Rd, Vancouver, BC V6T 1Z1, Canada*
[13]*Astronomical Observatory of the University of Geneva, ch. d'Ecogia 16, CH-1290 Versoix, Switzerland*
[14]*Shanghai Key Lab for Astrophysics, Shanghai Normal University, 100 Guilin Road, 200234 Shanghai, China*
[15]*Department of Physics and Astronomy, University of Waterloo, Waterloo, ON N2L 3G1, Canada*
[16]*Perimeter Institute for Theoretical Physics, 31 Caroline St N., Waterloo, ON N2L 2Y5, Canada*

Accepted 2015 August 30. Received 2015 August 28; in original form 2015 July 15

ABSTRACT

We present weak lensing constraints on the ellipticity of galaxy-scale matter haloes and the galaxy-halo misalignment. Using data from the Canada–France–Hawaii Telescope Lensing Survey (CFHTLenS), we measure the weighted-average ratio of the aligned projected ellipticity components of galaxy matter haloes and their embedded galaxies, $f_{\rm h}$, split by galaxy type. We then compare our observations to measurements taken from the Millennium Simulation, assuming different models of galaxy-halo misalignment. Using the Millennium Simulation, we verify that the statistical estimator used removes contamination from cosmic shear. We also detect an additional signal in the simulation, which we interpret as the impact of intrinsic shape–shear alignments between the lenses and their large-scale structure environment. These alignments are likely to have caused some of the previous observational constraints on $f_{\rm h}$ to be biased high. From CFHTLenS, we find $f_{\rm h} = -0.04 \pm 0.25$ for early-type galaxies, which is consistent with current models for the galaxy-halo misalignment predicting $f_{\rm h} \simeq 0.20$. For late-type galaxies we measure $f_{\rm h} = 0.69^{+0.37}_{-0.36}$ from CFHTLenS. This can be compared to the simulated results which yield $f_{\rm h} \simeq 0.02$ for misaligned late-type models.

Key words: gravitational lensing: weak – galaxies: haloes.

1 INTRODUCTION

In the standard cosmological paradigm, ΛCDM, galaxies, groups, and clusters are embedded in large haloes of – mostly dark – matter. Numerical simulations of cosmic structure formation predict that these haloes are roughly triaxial (e.g. Jing & Suto 2002), and that their average density profiles closely follow the Navarro–Frenk–White profile (NFW; Navarro, Frenk & White 1996, 1997). In projection, these should approximately appear elliptical. This prediction can be tested observationally on the scales of galaxies and clusters. One approach is to constrain halo shapes via the use of baryonic tracers such as satellite galaxies (e.g. Holmberg 1969; Brainerd 2005; Libeskind et al. 2005; Yang et al. 2006; Azzaro

⋆ E-mail: schrabba@astro.uni-bonn.de

et al. 2007; Faltenbacher et al. 2007, 2009; Metz, Kroupa & Jerjen 2007; Bailin et al. 2008; Okumura, Jing & Li 2009; Agustsson & Brainerd 2010; Nierenberg et al. 2011), the distribution of stellar velocity (Olling & Merrifield 2000), satellite tidal streams (Ibata et al. 2001; Lux et al. 2012; Vera-Ciro & Helmi 2013), HI gas (Banerjee & Jog 2008; O'Brien, Freeman & van der Kruit 2010), or planetary nebulae (Napolitano et al. 2011). Such constraints can be compared to the output of hydrodynamical simulations that aim at modelling galaxy formation, linking the baryonic and dark matter components, and which can provide predictions on the relative (mis-) alignment of galaxies, their dark matter hosts, and the surrounding large-scale structure, as well as on the impact of the baryons on halo shapes (e.g. Bailin et al. 2005; Knebe et al. 2010; Vera-Ciro et al. 2011; Tenneti et al. 2014; Debattista et al. 2015; Laigle et al. 2015; Velliscig et al. 2015).

As an observational alternative, gravitational lensing probes the total projected mass distribution directly without relying on visible tracers. Strong gravitational lensing can provide information on the inner shapes of the mass distribution in massive clusters (e.g. Limousin et al. 2013) and galaxies (van de Ven et al. 2010; Dutton et al. 2011; Suyu et al. 2012), but at these scales baryons have a non-negligible influence. At larger scales, constraints on the projected mass distribution can be obtained with weak gravitational lensing, which probes the coherent distortions imprinted on to the observed shapes of background galaxies by the tidal gravitational field (e.g. Bartelmann & Schneider 2001; Schneider 2006). Even at these scales, baryons contribute to the total mass distribution probed by weak lensing (e.g. in the form of satellite galaxies), but the dark matter is expected to dominate.

Weak gravitational lensing has been successfully used in a wide range of applications, including for example cosmic shear studies which are sensitive to the growth of large-scale structure (e.g. Schrabback et al. 2010; Kilbinger et al. 2013; Heymans et al. 2013; Huff et al. 2014; Kitching et al. 2014; Simon et al. 2015), the mass calibration of galaxy clusters (e.g. von der Linden et al. 2014; Ford et al. 2015; Hoekstra et al. 2015; Kettula et al. 2015), and constraints on the *azimuthally averaged* mass profiles of galaxy matter haloes (e.g. Mandelbaum et al. 2006b; van Uitert et al. 2011; Leauthaud et al. 2012; Velander et al. 2014; Hudson et al. 2015).

In principle, weak lensing is also sensitive to halo ellipticity as the gravitational shear at a given radius is larger along the direction of the major axis of the projected halo compared to the projected minor axis (e.g. Brainerd & Wright 2000; Natarajan & Refregier 2000). For very massive clusters, the weak lensing signal is strong enough to provide individual halo ellipticity constraints (Corless, King & Clowe 2009; Oguri et al. 2010). Constraints were also obtained in stacked analyses of larger cluster samples (Evans & Bridle 2009; Oguri et al. 2012). For less massive, galaxy-scale haloes, the signal can still be detected statistically by stacking very large samples.

A measurement of this effect through stacking requires one to align the shear field around all lenses prior to stacking, such that the major axes of all projected haloes are aligned. The orientations of the (mostly dark) matter haloes, however, are not directly observable. One approach which has been used instead for weak lensing halo shape studies, is to approximate the orientations of the projected haloes by the orientations of their galaxy images (Hoekstra, Yee & Gladders 2004; Mandelbaum et al. 2006c; Parker et al. 2007; van Uitert et al. 2012). Also, it has typically been assumed that, on average and in projection, more elliptical lenses are hosted by more elliptical haloes, as supported by simulations for early-type galaxies (Novak et al. 2006). A key parameter which is then extracted is the average aligned ellipticity ratio between the ellipticities of the projected halo and the observed lens light distribution $f_{\rm h} = \langle \cos(2\Delta\phi_{\rm h,\,g})|e_{\rm h}|/|e_{\rm g}|\rangle$, where the averaging typically includes a weighting scheme that depends on $|e_{\rm g}|$. Here, $\Delta\phi_{\rm h,\,g}$ is the angle between the major axis of the projected galaxy light distribution and the major axis of its projected matter halo. Thus, only in the case of perfect alignment ($\Delta\phi_{\rm h,\,g} = 0$), $f_{\rm h}$ reduces to the actual ellipticity ratio. However, in practice one expects a considerable random misalignment between the observed shapes of galaxies and matter haloes, as suggested both by numerical simulations of galaxy formation (e.g. Okamoto et al. 2005; Crain et al. 2009; Bett et al. 2010; Deason et al. 2011; Dong et al. 2014; Tenneti et al. 2014; Wang et al. 2014) and observations that approximate matter haloes via the distribution of satellites (e.g. Okumura et al. 2009). This should substantially reduce $f_{\rm h}$ and wash out the halo shape signature, making it difficult to detect observationally (Bett 2012). It is important to test this prediction observationally, both to improve our understanding of galaxy formation, but also to inform models of intrinsic galaxy alignments. Such alignments of galaxies with their surrounding mass distribution are an important physical contaminant for cosmic shear studies (e.g. Heymans et al. 2013; Joachimi et al. 2013b). Of particular concern are shape–shear intrinsic alignments (Hirata & Seljak 2004). Here, the ellipticities of foreground galaxies are aligned with their surrounding large-scale structure, which lenses the background sources. So far, most constraints on shape–shear alignments come from studies investigating the alignment of galaxies with their surrounding galaxy distribution (e.g. Joachimi et al. 2011; Mandelbaum et al. 2011; Li et al. 2013; Zhang et al. 2013; Singh, Mandelbaum & More 2015). Interestingly, the aligned halo shape signature we want to extract directly contributes to the shape–shear intrinsic alignment signal at small scales (Bridle & Abdalla 2007).

In addition to the expected small signal, there are further observational challenges: while a potential additional alignment of lenses and sources does not affect the azimuthally averaged galaxy–galaxy lensing signal, this is no longer the case for the most simple estimator of the anisotropic halo ellipticity signal. Such a source-lens alignment can, for example, be introduced by incomplete removal of instrumental signatures such as the point spread function (PSF). In addition, gravitational lensing by structures in front of the lens causes extra alignment. The latter is commonly referred to as cosmic shear, or sometimes as multiple deflections (Brainerd 2010). For example, Howell & Brainerd (2010) study the impact of cosmic shear on halo ellipticity constraints and conclude that observational estimates of the ratio of the shears along the lens major and minor axes would need to be compared to Monte Carlo simulations for interpretation. However, they do not consider the modified estimator introduced by Mandelbaum et al. (2006c, hereafter M06), which leads to a cancellation of such spurious signal at the relevant (small) scales, and which we employ in the current study.

Previous observational constraints on halo ellipticity from weak lensing are somewhat inconclusive: On the one hand, Hoekstra et al. (2004) and Parker et al. (2007) find indications for positive $f_{\rm h}$ using magnitude-selected lens samples and simple estimators that do not correct for systematic shear. On the other hand M06 and van Uitert et al. (2012) separate lenses by colour and correct for systematic shear, but do not detect significantly non-zero $f_{\rm h}$. For example M06 find $f_{\rm h} = 0.60 \pm 0.38$ for red and $f_{\rm h} = -1.4^{+1.7}_{-2.0}$ for blue lenses using data from the Sloan Digital Sky Survey (SDSS). Very recently, Clampitt & Jain (2015) reported a significant detection of the signature of halo ellipticity around luminous red galaxies (LRGs), also employing SDSS data.

In this study we use weak lensing data from the Canada-France-Hawaii Telescope Lensing Survey (CFHTLenS; Heymans et al. 2012; Hildebrandt et al. 2012; Erben et al. 2013; Miller et al. 2013) to derive updated constraints on the ellipticity of galaxy matter haloes from weak lensing. These data allow us to constrain the signal for galaxies subdivided into bins of photometric type and stellar mass. The former division allows us to approximately separate the lens sample into early- and late-type galaxies, which have different predictions for the expected weak lensing halo shape signal. The latter division optimizes the total measurement signal-to-noise as stellar mass acts as a proxy for halo mass and therefore the signal strength.

In addition, we study a simulated weak lensing halo shape signal based on the Millennium Simulation (Springel et al. 2005), employing the ray-tracing analysis from Hilbert et al. (2009) and lens shapes computed in Joachimi et al. (2013a,b). On the one hand, this provides a signal prediction given current galaxy-halo (mis-) alignment models (Bett 2012) that we can compare the CFHTLenS results to. On the other hand, it allows us to study the impact of cosmic shear on the measurement and check for deviations from the simple model prediction of isolated elliptical NFW haloes.

This paper is organized as follows: Section 2 describes the formalism of the halo ellipticity measurements using weak lensing, and the verification tests which we have conducted using a simple simulation. In Section 3, we summarize properties of the CFHTLenS data, discuss the selection of lens and source galaxies, and present the measured shear signal and constraints on the aligned ellipticity ratio f_h. We present our analysis of the simulated data based on the Millennium Simulation in Section 4. We then discuss our results and conclude in Section 5. In addition, we present a consistency check for shape measurements of background sources in the vicinity of bright foreground lenses using image simulations in Appendix A.

For the computation of angular diameter distances we by default assume a flat ΛCDM cosmology with $\Omega_\mathrm{m} = 0.3$, $\Omega_\Lambda = 0.7$, $H_0 = 70 h_{70}$ km s^{-1} Mpc^{-1}, and $h_{70} = 1$, which is consistent with the best-fitting cosmological parameters from both WMAP9 (Hinshaw et al. 2013) and *Planck* (Planck Collaboration et al. XIII 2015) at the $\sim 1\sigma$–2σ level. The only exception is our analysis of the simulated data from the Millennium Simulation, for which we use the input cosmological parameters of the simulation $\Omega_\mathrm{m} = 0.25$, $\Omega_\Lambda = 0.75$, $H_0 = 73 h_{73}$ km s^{-1} Mpc^{-1}, and $h_{73} = 1$ (Springel et al. 2005). All magnitudes are in the AB system. Stellar masses M_* are given in units of solar masses $\mathrm{M}_\odot$.

2 METHOD

2.1 Formalism

The methodology of our analysis largely follows the approach and notation that was introduced by M06 and additionally applied in van Uitert et al. (2012). It allows for the correction of spurious signal originating from cosmic shear or instrumental distortions.

2.1.1 *Constraining the isotropic galaxy–galaxy lensing signal*

In weak lensing studies the shape of a galaxy is typically described by the complex ellipticity

$$e = e_1 + \mathrm{i} e_2 = |e| \mathrm{e}^{2\mathrm{i}\phi} \,. \tag{1}$$

For the ellipticity definition employed here (see Miller et al. 2013)[1] and the case of an idealized source with elliptical isophotes, the absolute value of the ellipticity is given by $|e| = (a - b)/(a + b)$. Here, a and b are the major and minor axes of the ellipse, while ϕ corresponds to the position angle of the major axis from the x-axis of the coordinate system. In this definition the ellipticity of each background galaxy provides an unbiased but very noisy estimate of the reduced gravitational shear g in the direction of the source:

$$E(e) = g = \frac{\gamma}{1 - \kappa} \simeq \gamma \,, \tag{2}$$

where E indicates the expectation value, while γ and κ denote the shear and convergence. In principle, all structures along the line of sight from the source to the observer contribute to the net shear and convergence (see e.g. Schneider 2006). However, in galaxy–galaxy weak lensing analyses, such as the study presented here, one correlates the shear inferred from background sources with the positions of foreground lenses. In this case, only structures at the lens redshift contribute to the net signal (other structures add noise[2]), allowing us to express the correlated convergence $\kappa = \Sigma / \Sigma_\mathrm{c}$ as the ratio between the surface mass density Σ and the critical surface mass density:

$$\Sigma_\mathrm{c} = \frac{c^2}{4\pi G} \frac{1}{D_\mathrm{l}\, \beta} \,. \tag{3}$$

Here, c denotes the speed of light in vacuum and G the gravitational constant. The geometric lensing efficiency β is defined as

$$\beta = \max \left[0, \frac{D_\mathrm{ls}}{D_\mathrm{s}} \right] \,. \tag{4}$$

D_s, D_l, and D_ls indicate the physical angular diameter distances to the source, to the lens, and between lens and source, respectively (note that the equations in M06 are expressed for comoving distances instead).

Galaxy–galaxy weak lensing analyses study the stacked shear field around foreground lens galaxies. For this it is useful to decompose the shear and correspondingly the ellipticities of background galaxies into the tangential component and the 45°-rotated cross component:

$$e_\mathrm{t} = -e_1 \cos 2\theta - e_2 \sin 2\theta \,, \tag{5}$$

$$e_\times = +e_1 \sin 2\theta - e_2 \cos 2\theta \,, \tag{6}$$

where θ is the azimuthal angle with respect to the lens position as measured from the x-axis of the coordinate system used.

The majority of the previous galaxy–galaxy weak lensing analyses have only studied the profile of the azimuthally averaged tangential shear γ_t, which relates to the differential surface mass density profile $\Delta\Sigma(r) \equiv \bar{\Sigma}(<r) - \Sigma(r)$, where $\bar{\Sigma}(<r)$ is the mean convergence within radius r, as $\Delta\Sigma = \gamma_\mathrm{t} \Sigma_\mathrm{c}$. We estimate the differential surface density from the source galaxy ellipticities as

$$\widehat{\Delta\Sigma}(r) = \frac{\sum_i w_i \Sigma_{\mathrm{c},i}^{-2} \left(e_{\mathrm{t},i} \Sigma_{\mathrm{c},i} \right)}{\sum_i w_i \Sigma_{\mathrm{c},i}^{-2}} = \frac{\sum_i w_i \Sigma_{\mathrm{c},i}^{-1} e_{\mathrm{t},i}}{\sum_i w_i \Sigma_{\mathrm{c},i}^{-2}} \,, \tag{7}$$

[1] This ellipticity definition is often referred to as ϵ in the literature. Here, we denote it as e to be consistent with Miller et al. (2013).

[2] For a weak lensing halo shape analysis, foreground structures in front of the lens cause an extra alignment of sources and lenses, which does introduce spurious signal for simple estimators. However, this signal is accounted for via the formalism explained further below in this section.

where we sum over lens–source pairs in an annulus around r. In this section, we indicate estimators with a hat for clarity, but we drop it in the subsequent sections when presenting results. In our analysis, we employ inverse-variance weights w_i for the source shape estimates. These weights account for both measurement noise and the intrinsic ellipticity distribution (Miller et al. 2013). We use uniform source shape weights for simulated data. The main reason for conducting the analysis in terms of $\Delta\Sigma$, which is a rescaled version of the shear, instead of the shear directly, is to adequately account for the redshift dependence of the weak lensing signal.

We note that the tangential ellipticity components e_t of sources provide estimates for the tangential component of the reduced shear g_t, while $\Delta\Sigma$ is defined in terms of the tangential component of shear γ_t. In galaxy–galaxy weak lensing, typically $|\gamma| \ll 1$ and $|\kappa| \ll 1$. Hence, many studies have typically approximated the reduced shear with the shear as indicated in equation (2). Here we implicitly account for the difference when fitting the azimuthally averaged tangential shear profiles, as we find a small but non-negligible impact for our most massive lenses. When studying the anisotropy in the shear field, as detailed below, we however ignore reduced shear corrections as they cancel out to leading order.

In our analysis, we fit the isotropic part of the measured shear profile with an NFW shear profile prediction according to Wright & Brainerd (2000) in order to constrain $r_{200\mathrm{c}}$, the radius corresponding to a mean overdensity that is 200 times the critical density at the lens redshift, from the data itself. For this, we employ the mass–concentration relation of NFW haloes from Duffy et al. (2008).

2.1.2 *Constraining the anisotropic galaxy-galaxy lensing signal*

The formalism to study the anisotropic weak lensing shear field around elliptical lenses was introduced by Natarajan & Refregier (2000) for the case of an elliptical isothermal sphere, and further developed and generalized for other density profiles in M06. Here, we largely follow the notation from M06, and introduce a few additional quantities.

Similarly to M06, we model the stacked and scaled tangential shear field as a combination of an isotropic profile $\Delta\Sigma_\mathrm{iso}(r)$ and some azimuthal variation as

$$\Delta\Sigma_\mathrm{model}(r, \Delta\theta) = \Delta\Sigma_\mathrm{iso}(r)\left[1 + 4 f_\mathrm{rel}(r)|e_\mathrm{h,a}|\cos(2\Delta\theta)\right] . \quad (8)$$

Here, $\Delta\theta$ denotes the position angle with respect to the major axis of the lens galaxy. We do not know the orientations of the matter halo ellipticities e_h on the sky. Thus, we have to approximate them with the orientations of their corresponding galaxy ellipticities e_g when stacking the anisotropic shear field. Accordingly, our analysis is only sensitive to the average component

$$|e_\mathrm{h,a}| = \langle\cos(2\Delta\phi_\mathrm{h,g})|e_\mathrm{h}|\rangle \simeq \langle\cos(2\Delta\phi_\mathrm{h,g})\rangle|e_\mathrm{h}| \quad (9)$$

of the halo ellipticity that is aligned with the galaxy ellipticity, where $\Delta\phi_\mathrm{h,\,g}$ indicates the misalignment angle. Here, we average over the misalignment distribution, which we assume does not depend on $|e_\mathrm{h}|$. Following M06, we make the assumption that the absolute value of the halo ellipticity is proportional to the absolute value of the galaxy ellipticity

$$|e_\mathrm{h}| = \tilde{f}_\mathrm{h}|e_\mathrm{g}| . \quad (10)$$

While there will be deviations from this assumed linear scaling in reality, it provides a reasonable approximate weighting scheme (see also van Uitert et al. 2012, who explore additional schemes).

In equation (8), $f_\mathrm{rel}(r)$ describes the relative asymmetry in the shear field for an elliptical halo of ellipticity $|e_\mathrm{h,\,a}|$. It depends on the assumed density profile and needs to be computed numerically for non-power-law profiles (see M06).[3] To recover the notation of M06, we define

$$f_\mathrm{h} = \tilde{f}_\mathrm{h}\langle\cos(2\Delta\phi_\mathrm{h,g})\rangle = \frac{|e_\mathrm{h}|}{|e_\mathrm{g}|}\langle\cos(2\Delta\phi_\mathrm{h,g})\rangle , \quad (11)$$

$$f(r) = f_\mathrm{rel}(r) f_\mathrm{h} . \quad (12)$$

Then, equation (8) reduces to

$$\Delta\Sigma_\mathrm{model}(r, \Delta\theta) = \Delta\Sigma_\mathrm{iso}(r)\left[1 + 4 f(r)|e_\mathrm{g}|\cos(2\Delta\theta)\right] . \quad (13)$$

M06 show that the joint solution for the estimators of the isotropic and anisotropic shear field components is given by

$$\widehat{\Delta\Sigma_\mathrm{iso}}(r) = \frac{\sum_i w_i \Sigma_{\mathrm{c},i}^{-1} e_{\mathrm{t},i}}{\sum_i w_i \Sigma_{\mathrm{c},i}^{-2}} , \quad (14)$$

$$\widehat{f(r)\Delta\Sigma_\mathrm{iso}}(r) = \frac{\sum_i w_i \Sigma_{\mathrm{c},i}^{-1} e_{\mathrm{t},i}|e_{\mathrm{g},i}|\cos(2\Delta\theta_i)}{4\sum_i w_i \Sigma_{\mathrm{c},i}^{-2}|e_{\mathrm{g},i}|^2\cos^2(2\Delta\theta_i)} , \quad (15)$$

where the summation is again over lens–source pairs in a separation interval around r. Note that the factor 2 difference in equations (13) and (15) compared to equations (4) and (6) in M06 originates from the different ellipticity definition used by M06. To ease the comparison to M06 we decided to not rescale $f(r)$, but rather to write out the factor 2 difference explicitly.

In practice, (15) is not a useful estimator for constraining halo ellipticity as it is susceptible to a systematic signal if the ellipticities of lenses and sources are aligned because of an additional effect. This could arise from instrumental systematics such as imperfectly corrected PSF anisotropy, but also from cosmic shear by structures in front of the lens. This can easily be understood: for example, an intrinsically round lens (with an isotropic halo) would appear elliptical because of this extra shear or systematic. Sources would also have an extra shear component parallel to the lens ellipticity. In the coordinates defined by the observed lens ellipticity this appears as an increased shear along the lens minor axis and a decreased shear along the lens major axis. Accordingly, this would be interpreted as an 'anti-aligned' halo with $f_\mathrm{h} < 0$.

To cancel this systematic contribution, M06 suggest to include an additional term in the estimator that is based on the ellipticity cross component $e_\times$ (6), and which is given by

$$\widehat{f_{45}(r)\Delta\Sigma_\mathrm{iso}}(r) = -\frac{\sum_i w_i \Sigma_{\mathrm{c},i}^{-1} e_{\times,i}|e_{\mathrm{g},i}|\sin(2\Delta\theta_i)}{4\sum_i w_i \Sigma_{\mathrm{c},i}^{-2}|e_{\mathrm{g},i}|^2\sin^2(2\Delta\theta_i)} . \quad (16)$$

Equations (13) and (16) obtain nearly equal contributions from systematic effects aligning the lens and source ellipticities, as long as the shear correlation function $\xi_-(r) = \langle\tilde{\gamma}_\mathrm{t}\tilde{\gamma}_\mathrm{t} - \tilde{\gamma}_\times\tilde{\gamma}_\times\rangle(r)$ is sufficiently small, where $\tilde{\gamma}$ indicates the additional 'systematic' shear. This is the case at the relevant small r (see our test for cosmic shear in Section 4, and the discussion in M06). Hence, the estimator $(f(r) - \widehat{f_{45}(r)})\,\Delta\Sigma_\mathrm{iso}(r)$ can be used to probe halo ellipticity free from the systematic contribution.

Importantly, $f_{45}(r)$ also contains signal from the flattened halo, so that both $f(r)$ and $f_{45}(r)$ need to be modelled. Here we scale the model for $f_{45}(r)$ in correspondence to equation (12) as

$$f_{45}(r) = f_{\mathrm{rel},45}(r) f_\mathrm{h} . \quad (17)$$

[3] Our tests conducted in Section 2.2 indicate that there is only a weak dependence of $f_\mathrm{rel}(r)$ on the halo ellipticity itself, which can be ignored for the expected halo ellipticities.

M06 compute predictions for $f_{\rm rel}(r)$ and $f_{\rm rel,\,45}(r)$ for several elliptical density profiles numerically. We restrict our analysis to elliptical NFW profiles as they provide good fits to the isotropic shear signal of the CFHTLenS data within the considered radial range, see Section 3.5.1. For NFW density profiles M06 compute model predictions in terms of $r/r_{\rm s}$, where $r_{\rm s}$ is the NFW scale radius (we linearly interpolate between the discrete values provided by M06). Accordingly, $f_{\rm rel}(r)$ and $f_{\rm rel,\,45}(r)$ can be computed for arbitrary NFW profiles and halo masses. We verify the numerical predictions from M06 in Section 2.2, where we find very good agreement with M06 for $f_{\rm rel}(r)$. However, our analysis indicates an opposite sign for $f_{\rm rel,\,45}(r)$ compared to the M06 models[4] (see Section 2.2). Hence, while we use the model interpolation scheme from M06, we implicitly use an opposite sign for $f_{\rm rel,\,45}(r)$.

2.1.3 *Estimating* $\mathrm{f_h}$

It is a primary goal of our analysis to constrain the aligned ellipticity ratio $f_{\rm h}$. From the estimators in equations (14), (15), and (16), and from the model descriptions in equations (12) and (17), one could be tempted to define an estimator as

$$\widehat{f_{\rm h}^{\rm biased}}(r) = \frac{\widehat{y}(r)}{\widehat{x}(r)} \tag{18}$$

with

$$\widehat{y}(r) = \frac{1}{f_{\rm rel}(r) - f_{\rm rel,45}(r)} (f - \widehat{f_{45}})\,\widehat{\Delta\Sigma_{\rm iso}}(r)\,, \tag{19}$$

$$\widehat{x}(r) = \widehat{\Delta\Sigma_{\rm iso}}(r)\,. \tag{20}$$

However, the estimator in equation (18) would be biased due to the occurrence of the noisy $\widehat{x}(r)$ in the denominator. In addition, we want to combine the estimates from the different radial bins, and possibly also different galaxy samples. One solution could be to divide by the best-fitting model for $\Delta\Sigma_{\rm iso}(r)$, e.g. obtained from an NFW shear profile fit. However, here we adopt the alternative approach suggested by M06, which is based on Bliss (1935a,b) and Fieller (1954): we are interested in the ratio $m = y/x$ of two random variables. In our case, m corresponds to $f_{\rm h}$ assuming $f_{\rm rel}(r)$ and $f_{\rm rel,\,45}(r)$ model the relative asymmetry in the shear field well. We assume that y and x have a Gaussian distribution, which is a reasonable approximation in galaxy–galaxy lensing given the dominant shape noise. We have multiple estimators $\widehat{y}_i$, $\widehat{x}_i$ from the different radial bins. Also, in some cases, we want to combine the constraints from multiple galaxy samples originating from different redshift or stellar mass bins, which provide additional $\widehat{y}_i$, $\widehat{x}_i$. For each i, the quantity $\widehat{y}_i - m\widehat{x}_i$ is a Gaussian random variable drawn from an $N(\mu = 0, \sigma^2 = \tilde{w}_i^{-1})$ distribution with $\tilde{w}_i^{-1} = \sigma^2_{\widehat{y}_i} + m\sigma^2_{\widehat{x}_i}$. Accordingly, the summation

$$\frac{\sum_i \tilde{w}_i(\widehat{y}_i - m\widehat{x}_i)}{\sum_i \tilde{w}_i} \sim N\left(0, \frac{1}{\sum_i \tilde{w}_i}\right) \tag{21}$$

over all measurements is also a Gaussian random variable, where the distribution is taken at fixed m. We then determine frequentist confidence intervals at the $Z\sigma$ level as

$$\frac{-Z}{\sqrt{\sum_i \tilde{w}_i}} < \frac{\sum_i \tilde{w}_i(\widehat{y}_i - m\widehat{x}_i)}{\sum_i \tilde{w}_i} < \frac{Z}{\sqrt{\sum_i \tilde{w}_i}}\,. \tag{22}$$

By stepping through a grid in m we identify the best-fitting value that provides the desired estimator

$$\widehat{f}_{\rm h} = m(Z = 0)\,, \tag{23}$$

as well as 68 per cent confidence limits $m(Z = \pm 1)$. At the best-fitting $m(Z = 0)$ we also compute a reduced χ^2 of the fit as

$$\chi^2/\mathrm{d.o.f.} = \frac{\sum_{i=1}^{i=n} \tilde{w}_i(\widehat{y}_i - m(Z=0)\widehat{x}_i)^2}{n-1}\,. \tag{24}$$

This approach assumes that off-diagonal covariance elements can be neglected. We find that this is indeed the case (see Sections 3.5.1 and 4.1).

2.2 Shear field of an elliptical NFW halo

In order to test our analysis pipeline and the model predictions from M06, we first analyse a simplistic simulation containing a single, elliptical NFW halo. A more detailed simulation is presented in Section 4, using data from the Millennium Simulation and including more realistic galaxy samples, galaxy misalignment, and cosmic shear.

For the basic test presented here, we generate an isotropic NFW convergence κ profile (Wright & Brainerd 2000) on a fine 4096^2 grid (10 arcmin × 10 arcmin) for a $M_{200c} = 10^{12}\,\mathrm{M}_\odot/h_{70}$ halo at $z_{\rm l} = 0.3$ assuming the Duffy et al. (2008) mass–concentration relation and sources at $z_{\rm s} = 1$. We shear the κ profile along the x-axis of the grid with various strengths to make it elliptical ($e_{\rm h,\,1} > 0$). Then the major and minor axes a and b of κ isodensity contours fulfil $|e_{\rm h}| = (a-b)/(a+b)$. Next, we compute the corresponding shear field using the Kaiser & Squires (1993) formalism. To test our fitting procedure with a regular covariance matrix we generate 50 shape noise realizations with a very small ellipticity dispersion (arbitrarily chosen $\sigma_{\rm e} = 0.004$), which were added to the shear field. For this test, we simply use the halo ellipticity as the lens ellipticity, hence $f_{\rm h} = 1$.

We plot the measured isotropic and anisotropic shear profiles for an $|e_{\rm h}| = 0.2$ halo in Fig. 1. The anisotropic signal (open symbols in the bottom panel) is well described by the best-fitting model using the M06 prescription once we account for the sign error for f_{45} (see Section 2.1). Here we accurately recover the input halo ellipticity ($f_{\rm h} = 1.002^{+0.003}_{-0.002}$). For comparison, we also show the measured signal if we artificially add a constant (scale independent) spurious alignment of the lens and sources corresponding to a shear of $\gamma_2 = 0.01$,[5] to roughly illustrate the effect of residual PSF anisotropy or cosmic shear (cross- and star-shaped symbols in the bottom panel of Fig. 1). While the $f\Delta\Sigma$ and $-f_{45}\Delta\Sigma$ components are individually disturbed, their combination $(f - f_{45})\Delta\Sigma$ is unaffected by the systematic shear as expected.

We repeat this analysis with various halo ellipticities $e_{\rm h}$ and plot the recovered $f_{\rm h}(e_{\rm h})$ in Fig. 2. This shows that the linear relation assumed in equations (12) and (17) is a good approximation, but leads to a slight overestimation of $f_{\rm h}$ for very elliptical haloes. However, as the deviations from $f_{\rm h} = 1$ are small for typical expected halo

[4] We note that different sign definitions exist in the literature for equation (6), which might have led to an inconsistent model prediction derived in M06.

[5] If we always orient the lens for this test along the x-axis (e_1 only), we need to apply a systematic shear along the uncorrelated 45°-rotated field diagonal (γ_2). We verified that we obtain identical results with a systematic shear along a random direction if we randomly rotate the lens and its shear field prior to applying the systematic shear. This would resemble reality more closely with random intrinsic lens orientations with respect to the orientation of the PSF or the cosmic shear field.

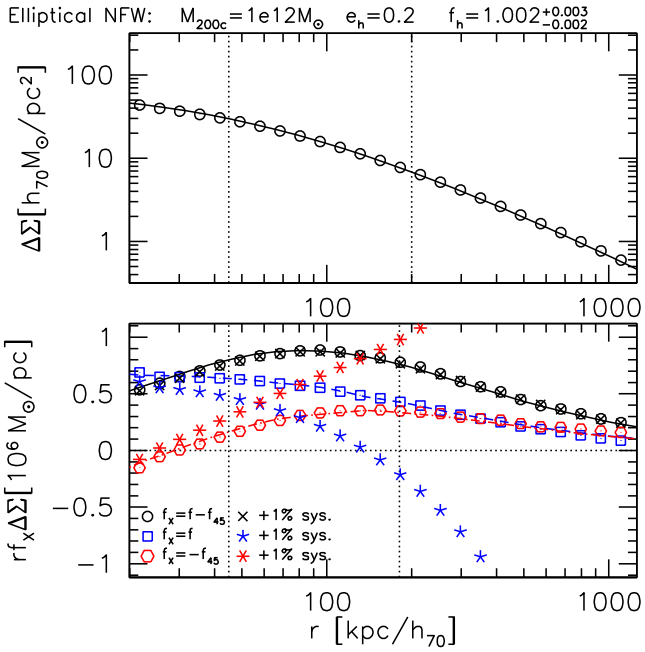

Figure 1. Test of the models and our analysis pipeline using a simple NFW κ profile for a $M_{200c} = 10^{12}\,M_\odot/h_{70}$ halo at $z_l = 0.3$ and $z_s = 1$ sources. The halo was sheared on a grid to an ellipticity $e_h = 0.2$ and the corresponding shear field was computed according to Kaiser & Squires (1993). The top and bottom panels show the isotropic and anisotropic shear profiles, respectively. For the anisotropic signal (note the scaling by r) the open blue squares, red hexagons, and black circles show $f\Delta\Sigma$, $-f_{45}\Delta\Sigma$, and $(f-f_{45})\Delta\Sigma$, respectively. The curves show corresponding model predictions from M06 for $e_h = 0.2$ and $f_h = 1$, where we have swapped the sign for the $-f_{45}$ model (see Section 2.1). The additional symbols show the same measured quantities, but with an extra constant 1 per cent shear added to both lens and source ellipticities (45° rotated from the lens orientation). The vertical dotted lines indicate the fit range.

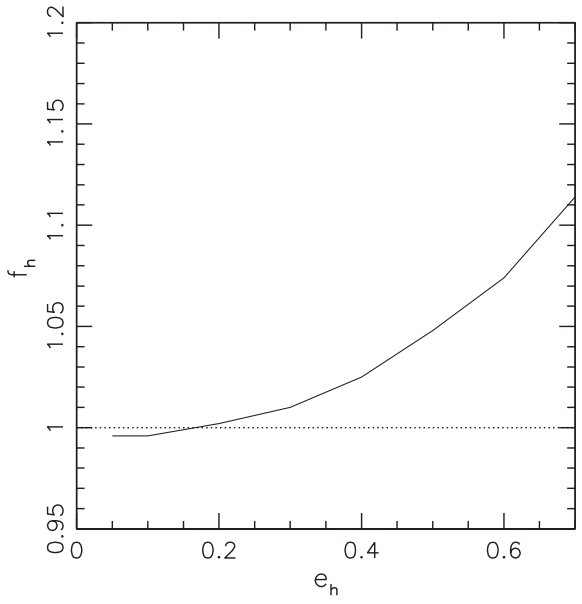

Figure 2. Test of the halo ellipticity recovery using the linearized elliptical shear field model from M06 (corrected for the sign inconsistency for f_{45}). Here the same type of elliptical NFW models was used as in Fig. 1, but for a range of halo ellipticities e_h. Perfect recovery corresponds to the dotted $f_h = 1$ line. Deviations for typical halo ellipticities are only a few per cent.

ellipticities[6] of $|e_h| \sim 0.2$, and given the large statistical uncertainties of CFHTLenS, we ignore this deviation in our analysis.

3 OBSERVATIONAL CONSTRAINTS FROM CFHTLenS

3.1 The CFHTLenS data

To constrain the aligned projected ellipticity ratio f_h observationally, we employ weak lensing data from the CFHTLenS. It has an effective area of 154 deg^2 imaged in the *ugriz* broad-band filters using MegaCam on CFHT with a 5σ limiting magnitude in the detection *i*-band and 2 arcsec apertures of $i_{AB} \sim 24.5$–24.7 (Erben et al. 2013). These data were obtained as part of the wide component of the Canada-France-Hawaii Telescope Legacy Survey (CFHTLS) which completed observations in early 2009.

The CFHTLenS team has reduced the imaging data using the THELI pipeline (Erben et al. 2009, 2013), measured PSF-corrected galaxy shapes in the *i*-band using *lens*fit (Miller et al. 2007, 2013; Kitching et al. 2008), and estimated photometric redshifts (photo-zs) from the *ugriz* data employing the BPZ algorithm (Benítez 2000; Coe et al. 2006) as detailed in Hildebrandt et al. (2012), with photo-z tests presented in Benjamin et al. (2013). Details on the CFHTLenS analysis pipeline and cosmology-independent systematic tests are presented in Heymans et al. (2012).

To subdivide the foreground lens galaxies in our analysis, we employ stellar mass estimates computed using LEPHARE (Arnouts et al. 1999; Ilbert et al. 2006). They are based on the stellar population synthesis (SPS) package of Bruzual & Charlot (2003) and assume a stellar initial mass function from Chabrier (2003). From this we built 18 templates with two different metallicities and nine exponentially decreasing star formation rates. We allow the dust extinction to vary between 0.05 to 0.3 mag using a Calzetti et al. (2000) extinction law, and 57 starburst ages ranging from 0.01 to 13.5 Gyr (for more details see section 2.1 of Velander et al. 2014).

3.2 KSB shapes for bright foreground galaxies

The *lens*fit shape measurement algorithm has been optimized to obtain accurate shape estimates for the typically faint and only moderately resolved distant source galaxies (Miller et al. 2013), as needed for an unbiased cosmological weak lensing analysis (e.g. Heymans et al. 2013; Kilbinger et al. 2013; Fu et al. 2014; Kitching et al. 2014). For our analysis of galaxy-halo shapes, we additionally require ellipticity estimates for the foreground lens galaxies. Many of these are fairly bright and extended, which may result in an exclusion of a galaxy during the *lens*fit shape analysis. This can be caused either because of a size comparable or exceeding the employed postage-stamp size (48 pixels), or outer isophotes significantly overlapping with neighbouring galaxies, or the presence of substantial substructure in the galaxy, which is not well described by the employed bulge+disc model (see Miller et al. 2013).

In order to not exclude these galaxies from our sample of lens galaxies, we perform shape measurements using the KSB algorithm originally proposed by Kaiser, Squires & Broadhurst (1995) and Luppino & Kaiser (1997). Based on weighted brightness moments this shape measurement algorithm is more robust to the presence of

[6] For example, in our analysis of haloes from the Millennium Simulation (see Section 4) that are populated by early-type galaxies, we find $\langle|e_h|\rangle = 0.163$, and only 0.5 per cent of the haloes have $|e_h| > 0.5$.

resolved substructure or nearby galaxies. Here, we employ the implementation of the algorithm detailed in Hoekstra et al. (1998) and Hoekstra, Franx & Kuijken (2000), which was tested in the blind challenges of the STEP project (Heymans et al. 2006a; Massey et al. 2007) and also employed for earlier weak lensing analyses of CFHTLS data (Hoekstra et al. 2006). While there are indications for remaining residual systematics in earlier cosmological weak lensing studies of CFHTLS data using KSB (Kilbinger et al. 2009; Heymans et al. 2012), we note that these are expected to mostly originate from poorly resolved, low signal-to-noise galaxies. In contrast, the studied lens galaxies have high signal to noise[7] and are well resolved. Thus, they are less sensitive to noise-related biases (e.g. Melchior & Viola 2012; Kacprzak et al. 2012; Refregier et al. 2012; Viola, Kitching & Joachimi 2014) and require smaller PSF corrections. Also see Sifón et al. (2015) where the KSB results for bright galaxies are compared to GALFIT shapes (Peng et al. 2002). Furthermore, as demonstrated in Section 2.2, additional ellipticity correlations between lenses and sources due to imperfect PSF anisotropy correction or cosmic shear cancel out in the analysis at the relevant scales thanks to the employed estimator. Thus, the application of KSB shapes for lens galaxies without *lens*fit shapes does not compromise the systematic accuracy of our measurement, but only increases the statistical precision. Note that differing from earlier KSB studies of CFHTLS data, we conduct galaxy shape measurements on individual exposures and not stacks, similarly to the *lens*fit analysis, and combine the shape estimates on the catalogue level as the weighted mean estimate.

3.3 Lens sample

To obtain a sample of foreground lens galaxies, we preselect relatively bright objects ($i < 23.5$) that are resolved (CLASS_STAR < 0.5, star_flag $= 0$, non-zero shape weights from *lens*fit or KSB) and feature a single-peaked photometric redshift probability distribution function (ODDS > 0.9; see Hildebrandt et al. 2012). We select lenses within the range of best-fitting photometric redshifts $0.2 < z_\mathrm{b} < 0.6$, which we subdivide into four lens redshift slices of width $\Delta z_\mathrm{b} = 0.1$. We split the galaxies into red ($T_\mathrm{BPZ} \leq 1.5$) and blue lenses ($1.5 < T_\mathrm{BPZ} < 3.95$) using the photometric type T_BPZ from BPZ. In order to approximately sort the lenses by halo mass and optimize the measurement signal-to-noise ratio, we also subdivide them according to stellar mass $\log_{10}M_*$ as detailed in Table 1. When measuring the anisotropic shear signal, contributions from different lenses are weighted according to the lens ellipticity (see e.g. equation 15). Here, we restrict the analysis to lenses in the well-constrained ellipticity range $0.05 < |e_\mathrm{g}| < 0.95$.

An important aspect of our study is the direct comparison of our measurements from CFHTLenS to results from mock data based on the Millennium Simulation (see Section 4). For the mock data, we only have measurements for central haloes but not for satellites (see Section 4.2). To ensure that the results are comparable, we aim to minimize the fraction of satellites in our CFHTLenS lens samples. In addition, our model assumes that the anisotropic shear signal is caused by isolated elliptical NFW mass distributions (Section 2). This may be a reasonable approximation for centrals, but it is likely a poor descriptions for satellites embedded into a larger halo.

[7] In the highest redshift–redshift slice ($0.5 < z < 0.6$), the median signal-to-noise ratio defined as FLUX_AUTO/FLUXERR_AUTO from SEXTRACTOR is 181 (193) for the blue (red) lenses in the lowest stellar mass bins considered.

Table 1. Overview over the subsample of lens galaxies used – Column 1: split between red ($T_\mathrm{BPZ} \leq 1.5$) and blue lenses ($1.5 < T_\mathrm{BPZ} < 3.95$) using the photometric type T_BPZ from BPZ. Column 2: stellar mass range. Column 3: number of selected lenses in the redshift interval $0.2 \leq z_\mathrm{l} < 0.6$. Column 4: ellipticity dispersion of the selected lenses with $0.05 < |e_\mathrm{g}| < 0.95$ combining both ellipticity components.

Colour	Stellar mass [$\mathrm{M}_\odot$]	$N(0.2 \leq z_\mathrm{l} < 0.6)$	σ_e
Red	$10 < \log_{10} M_* < 10.5$	81 763	0.35
Red	$10.5 < \log_{10} M_* < 11$	93 032	0.30
Red	$\log_{10} M_* > 11$	25 982	0.23
Blue	$9.5 < \log_{10} M_* < 10$	166 604	0.38
Blue	$10 < \log_{10} M_* < 10.5$	91 692	0.36
Blue	$\log_{10} M_* > 10.5$	33 612	0.30

Velander et al. (2014) fit the isotropic galaxy–galaxy weak lensing signal around red and blue lenses in CFHTLenS using a halo model approach. They find that the satellite fraction is typically low both for blue lenses and for red lenses which have a high stellar mass. However, it increases steeply for red lenses towards lower stellar mass. To reduce the fraction of satellites in our sample, we therefore generally exclude red lenses with stellar mass $\log_{10}M_* < 10$. For the lowest stellar mass bin included in our analysis for red lenses ($10 < \log_{10}M_* < 10.5$), Velander et al. (2014) estimate a satellite fraction of $\alpha = 0.23 \pm 0.02$. To further reduce the fraction of satellites, we apply an additional cut to the galaxies in this bin using the internal flag from SEXTRACTOR (Bertin & Arnouts 1996). This removes any galaxy which is either partially blended with another object, or which has a nearby neighbour possibly affecting the measurement of the MAG_AUTO magnitude. Many of these galaxies are located close to a brighter early-type galaxy, as expected for satellites. We do not filter on this flag for the other stellar mass bins. In particular, this would exclude many bright early-type galaxies, which are presumably centrals but have faint nearby neighbours.

Given that the remaining fraction of satellites in our lens sample is low, we expect that they have a negligible impact on our results.[8] As consistency check for this we investigate the impact of the lens bin with the highest satellite fraction on our joint constraints in Section 3.5.2.

3.4 Source sample

From all galaxies with *lens*fit shape measurements and non-vanishing shape weights, we select those with a best-fitting photometric redshift in the range $z_\mathrm{l,\,upper} + 0.1 < z_\mathrm{b} < 1.3$ as our source background sample, where $z_\mathrm{l,\,upper}$ indicates the upper limit of the corresponding lens redshift slice. Above the upper limit at $z_\mathrm{b} = 1.3$ the *ugriz* CFHTLenS photometric redshifts become unreliable (Hildebrandt et al. 2012; Benjamin et al. 2013) with large redshift uncertainties and a partial contamination by low-redshift galaxies. Thus, we exclude these galaxies from our analysis to be

[8] A net alignment of satellites with respect to the tangential shear field of their parent halo could introduce spurious signal. However, we expect that this has a negligible impact on our study for the following reasons. First, the satellite fraction is low for our lens samples. Secondly, Sifón et al. (2015) place tight limits on the net alignment of cluster galaxies, showing that it must be very weak. Given our selection of lenses with relatively high stellar mass, we expect that many of the satellites present in the sample are actually cluster members. Finally, our analysis using $(f - f_{45})\Delta\Sigma$ reduces the impact of spurious alignment between lenses and sources, which also applies here to the first order.

conservative. As done by Velander et al. (2014), we further optimize the separation of lenses and sources by also removing source galaxies whose 95 per cent redshift confidence regions computed by BPZ overlap with the lens redshift slice. When we compute the galaxy–galaxy lensing signal we weight the contributions from the individual source galaxies according to their effective geometric lensing efficiency $\beta_i^{\rm eff} = \int \beta(z_{\rm l,c}, z_{\rm s}) p_i(z_{\rm s}) {\rm d}z_{\rm s}$. This is estimated from the full photometric redshift probability distributions of the sources $p_i(z_{\rm s})$ (see Hildebrandt et al. 2012) and uses the centre[9] of the thin lens redshift slice $z_{\rm l,\,c}$.

Miller et al. (2013) study the impact of noise bias for *lens*fit shape measurements and derive an empirical correction for multiplicative bias as a function of galaxy size and signal-to-noise ratio. Following Velander et al. (2014) we account for the net effect of this bias on the estimated shear profiles taking the individual shape weights and lensing efficiencies of the sources into account. We note that this bias correction cancels out for the halo ellipticity constraints except for its impact on the estimate of $r_{\rm 200c}$, which is used as upper limit for the fit range and to estimate $r_{\rm s}$ for the anisotropic shear field model.

Heymans et al. (2012) conduct a number of non-cosmological tests to flag CFHTLS fields which are likely affected by residual shape systematics. To be conservative, we base our primary analysis on the 129 out of 171 fields which pass these systematics tests[10] ('pass fields'), but for comparison we also provide constraints obtained from all fields. As explained in Section 2.1, the impact of both residual shape measurement systematics and foreground cosmic shear cancel out in our analysis as long as their shear correlation function ξ_- is sufficiently small on the scales of interest. As we will see in Section 4.3.4, this approach leaves negligible residuals from the expected cosmic shear signal. Accordingly, we expect that the fields classified as being useful for cosmic shear measurements can also be used to derive robust constraints on the aligned halo ellipticity.

3.5 Results

3.5.1 Measured signal and fit range

For each set of lens galaxies we measure the isotropic and anisotropic shear signal in 25 logarithmic bins of transverse physical separation between 20 kpc/h_{70} and 1.2 Mpc/h_{70}. We compute the signal separately for the lenses in each $\sim$1 deg^2 CFHTLS field, where we however use larger cut-outs from the mosaic catalogue of source galaxies to ensure a good coverage for the lenses close to the edge of a CFHTLS field. We then combine the signal from all fields according to their weight sums in each radial bin. Similarly, we compute a combined signal from all lens redshift slices for each field and the full survey. Figs 3 and 4 show the signal combining all redshift slices for the different stellar mass bins for red and blue lenses, respectively. Error bars are computed by bootstrapping the CFHTLS fields contributing to the combined survey signal. In this study, we are primarily interested in the relative asymmetry in the shear field. For detailed investigations of the isotropic galaxy–galaxy lensing signal in CFHTLenS, please see Velander et al. (2014), Hudson et al. (2015), and Coupon et al. (2015).

Before we can obtain constraints on the halo ellipticity we have to choose the radial range which is included in the fit. We are interested in the shape of the dark-matter-dominated matter halo surrounding the lens. Thus, we exclude small scales which are expected to be affected by the baryonic component of the lens. This is visible from the isotropic galaxy–galaxy lensing signal (see the top panels of Figs 3 and 4), showing a strong excess signal at small scales compared to the NFW fit constrained from larger scales (see also Velander et al. 2014; Hudson et al. 2015, who include a baryonic component in the fit to the isotropic signal).

In addition, the signal at very small scales might be influenced by systematic effects in the source detection and shape measurement process originating from the presence of the nearby bright foreground lens galaxies. As a first check for this we studied the relative azimuthal variation in the source density. Fig. 5 shows the radial dependence of $\sum_{i=1}^{N} \cos(2\Delta\theta_i)/N$ for all source–lens pairs in the highest stellar mass bins for both the blue and red lens samples, combining all redshift slices. The decrement at $r < 45$ kpc/h_{70} shows that we have a higher source density in the direction of the lens minor axis than the lens major axis. This suggests that either the object detection and deblending, or the shape measurement is more effective in the direction where the lens light has a smaller impact, which is not surprising. To ensure that this cannot affect our measurements we therefore only include radial scales $r > 45$ kpc/h_{70} for all lens bins, which also matches our goal to remove the scales where baryons are important. In Appendix A, we present an additional test for shape measurements close to bright lens galaxies using simulated galaxy images. It shows that any resulting spurious signal should be small compared to the statistical uncertainties from CFHTLenS within our fit range.

We also have to select an outer radius for the radial range which we include in the halo shape analysis. Here, we decide to include the signal out to $r_{\rm 200c}$. At significantly larger radii the isotropic galaxy–galaxy lensing signal shows an excess signal for the lower stellar mass bins (see the middle and right-hand panels in the top row of Fig. 3, showing excess signal at $r \gtrsim 1.6 r_{\rm 200c}$). Interpreted in the halo model (see e.g. Velander et al. 2014), this excess signal is a combination of the satellite term caused by the central galaxy (for lenses which are satellites) and the two-halo term from neighbouring haloes. Hence, at these scales the halo of the lensing galaxy can no longer be regarded as isolated, which would require a much more complicated modelling scheme. We note that the galaxy bins with higher stellar mass show only a weak excess signal at large radii, presumably due to a low satellite fraction. So while we could in principle extend the fit range for these galaxies slightly, we decided to use $r_{\rm 200c}$ as upper limit for all bins to keep the analysis more homogeneous.

Our approach requires that we first obtain an estimate for $r_{\rm 200c}$. For this, we fit the isotropic signal in the fixed radial range $45\,{\rm kpc}/h_{70} < r < 200\,{\rm kpc}/h_{70}$. Here we use the central redshift of our lenses $z_{\rm l} = 0.4$ when computing the isotropic NFW model for the combined analysis of all redshift slices.[11]

[9] We use the centre of the thin lens redshift slice instead of the individual best-fitting lens redshift for computational efficiency. We note that the influence is negligible for our study as verified by varying the width of the slices.

[10] See http://www.cadc-ccda.hia-iha.nrc-cnrc.gc.ca/community/CFHTLens/README_catalogs_release.txt.

[11] The central lens redshift agrees well with the effective lens redshift. The latter is computed according to the weight sums of the thin redshift slices for a fixed radial bin, yielding effective lens redshifts of 0.38–0.41 for the different galaxy types and stellar mass bins. We verified that the exact choice of the model $z_{\rm l}$ has minimal impact on our $f_{\rm h}$ constraints.

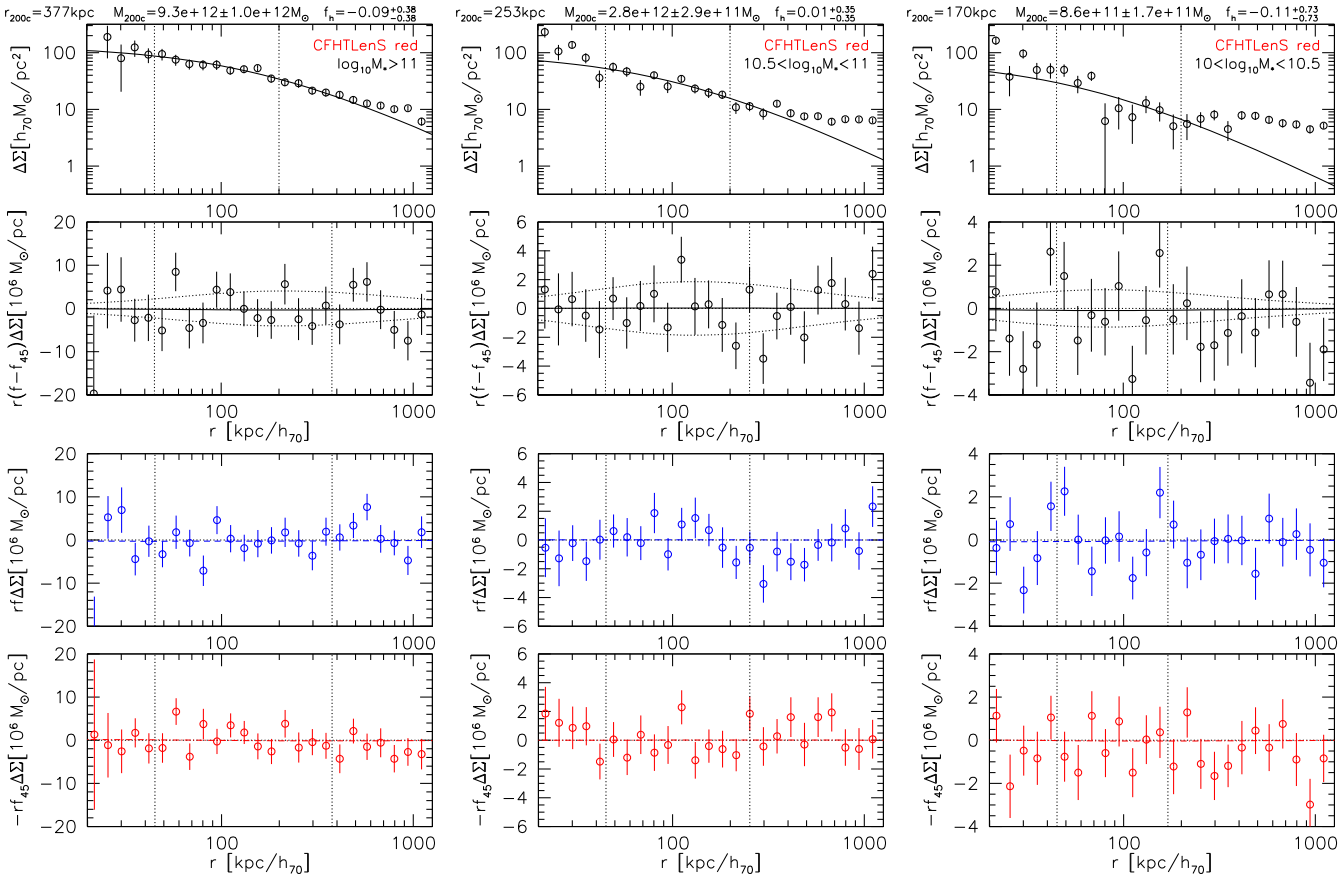

Figure 3. Measured isotropic (top row of panels) and anisotropic (rows two to four, note the varying y-axis scale) shear signal around red lenses in the CFHTLenS fields passing the systematics tests for cosmic shear as function of radial distance r. The anisotropic signal has been scaled by r for better readability, where rows two, three, and four show the signal components $(f-f_{45})\Delta\Sigma$, $f\Delta\Sigma$, and $-f_{45}\Delta\Sigma$, respectively. From left to right, we show the stellar mass bins $\log_{10}M_* > 11$, $10.5 < \log_{10}M_* < 11$, and $10 < \log_{10}M_* < 10.5$, combining all lens redshift slices. For the isotropic signal the curve shows the best-fitting NFW shear profile constrained within $45\,\mathrm{kpc}/h_{70} < r < 200\,\mathrm{kpc}/h_{70}$. For $(f-f_{45})\Delta\Sigma$ the curves show models corresponding to the best-fitting isotropic model and the best-fitting f_h (solid curves), as well as $f_\mathrm{h} \in \{+1, 0, -1\}$ (dotted curves) for comparison. For $f\Delta\Sigma$ and $-f_{45}\Delta\Sigma$, the dashed curves show model predictions for the best-fitting f_h. The best-fitting f_h has been constrained from $(f-f_{45})\Delta\Sigma$ and $\Delta\Sigma$ within $45\,\mathrm{kpc}/h_{70} < r < r_{200\mathrm{c}}$ (indicated by the vertical dotted lines), with $r_{200\mathrm{c}}$ estimated from the fit to the isotropic signal.

For comparison, we also plot the components of the anisotropic signal $f\Delta\Sigma$ and $-f_{45}\Delta\Sigma$ in the bottom panels of Figs 3 and 4. We note that the blue galaxies shown in Fig. 4 show a tendency for $f\Delta\Sigma < 0$ and $-f_{45}\Delta\Sigma > 0$, especially towards larger radii, which is consistent with the expected trend for cosmic shear. We will discuss this further in Section 5.

From the bootstrapping analysis we find that off-diagonal terms in the correlation matrix are small, justifying our analysis approach (see Section 2.1.3). Within the fit range of the isotropic signal the average of the off-diagonal elements is consistent with zero at the $\sim 1-2\sigma$ level for all lens bins with $|\langle \mathrm{cor}_{i,j}\rangle_{i>j}| \lesssim 2$ percent.

3.5.2 *Constraints on* f_h

The results of the fits to the CFHTLenS data are presented in Table 2 and we show the model fits to the data in Figs 3 and 4. For each lens colour and stellar mass bin we fit the combined shear signal from all redshift slices to ensure that the isotropic shear profile, which determines $r_{200\mathrm{c}}$, is measured with high significance.[12]

For none of the individual lens bins do we detect an f_h significantly different from zero. We also compute joint constraints from the $(f-f_{45})\Delta\Sigma$ and $\Delta\Sigma$ profiles of all stellar mass bins as explained in Section 2.1.3, yielding $f_\mathrm{h} = -0.04 \pm 0.25$ for the red lenses and $f_\mathrm{h} = 0.69^{+0.37}_{-0.36}$ for the blue lenses when restricting the analysis to the 129 fields passing the systematics tests described in Heymans et al. (2012, 'pass fields'). For comparison, we estimate $f_\mathrm{h} = -0.17 \pm 0.21$ for the red lenses and $f_\mathrm{h} = 0.56^{+0.34}_{-0.33}$ for the blue lenses when including all 171 CFHTLenS fields. In Table 2, we also list reduced χ^2 values which suggest that the models fit the data reasonably well in both cases when considering all lens bins together, but we note slightly lower χ^2/d.o.f. for the blue lenses when using the 'pass fields' only.

As a consistency check for the possible impact of satellite galaxies in the lens sample (see Section 3.3), we also compute joint constraints for the red lenses now excluding the stellar mass bin with the highest expected satellite fraction ($10 < \log_{10}M_* < 10.5$). In this case we obtain almost unchanged results $f_\mathrm{h} = -0.02 \pm 0.26$ for the 'pass fields' and $f_\mathrm{h} = -0.14 \pm 0.22$ for all fields, suggesting

[12] For comparison we repeated the measurement where we initially analyse each redshift slice separately and combine the constraints when estimating f_h. This led to nearly identical, and within the statistical uncertainty fully consistent results.

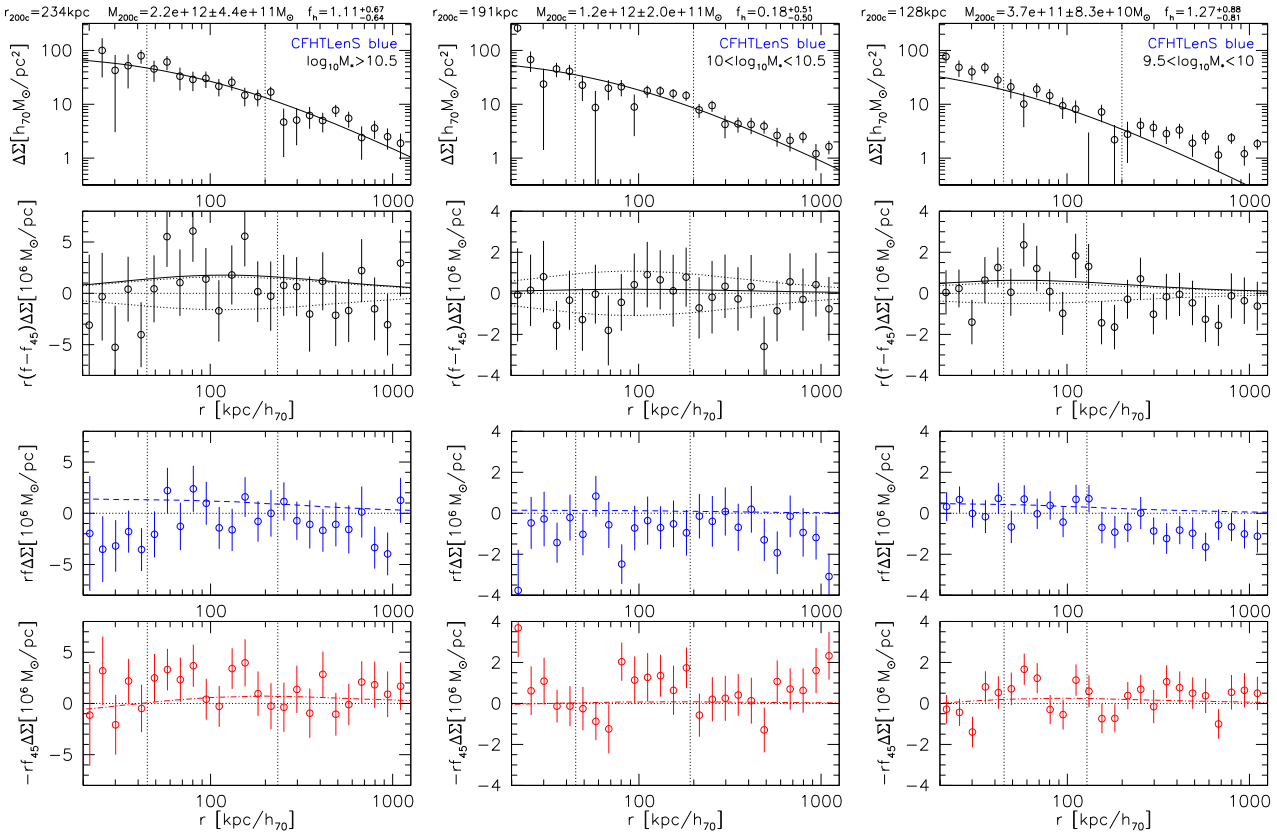

Figure 4. Measured isotropic (top panels) and anisotropic (rows two to four, note the varying y-axis scale) shear signal around blue lenses in the CFHTLenS fields passing the systematics tests for cosmic shear as function of radial distance r. From left to right, we show the stellar mass bins $\log_{10}M_* > 10.5$, $10 < \log_{10}M_* < 10.5$, and $9.5 < \log_{10}M_* < 10$, combining all lens redshift slices. For further details see the caption of Fig. 3.

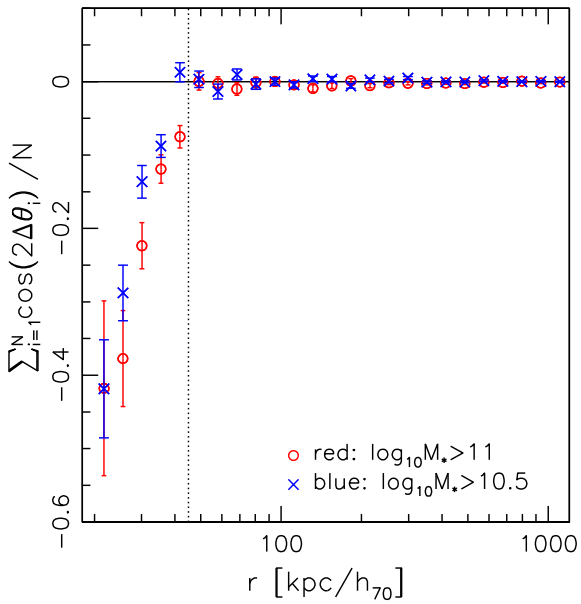

Figure 5. Measurement of the relative azimuthal variation in the source density in CFHTLenS with respect to the lens major axis as function of radial distance. The open red circles (blue crosses) show $\sum_{i=1}^{N}\cos(2\Delta\theta_i)/N$ for the red (blue) lenses in the correspondingly highest stellar mass bin combining all lens redshift slices. The decrement at $r < 45$ kpc/h_{70} indicates a higher source density in the direction of the lens minor axis compared to the major axis. To ensure that this cannot influence our analysis, we only include scales $r > 45$ kpc/h_{70} in the halo shape analysis.

that the remaining satellites have a negligible impact on the joint constraints.

4 ANALYSIS OF SIMULATED DATA BASED ON THE MILLENNIUM SIMULATION

To better understand the halo shape signal that we should expect from non-idealized haloes and in the presence of misalignments between galaxies and their matter haloes, we analyse a simulated data set based on ray-tracing through the Millennium Simulation (Springel et al. 2005) by Hilbert et al. (2009). This also allows us to test the correction for systematic shear (see Section 2.1) in the presence of a realistic cosmic shear field. We refer the reader to Hilbert et al. (2009) regarding the details of the ray-tracing. Here, we only summarize some of the main characteristics relevant for our analysis.

4.1 Mock shear catalogues

The simulated catalogues comprise 64 light cones, each with an area of 4×4 deg^2, which we subdivide into patches of 1 deg^2 to facilitate a bootstrap analysis similar to the CFHTLenS fields. We use all galaxies at $0.65 < z < 2.15$ as source sample ($z_{\rm median} = 1.187$), providing a high source density of 49.6 arcmin^{-2}. We wish to obtain high S/N estimates of the simulated halo shape signal and therefore add only small shape noise with $\sigma_{\rm e} = 0.03$, which was chosen to be of the same order as the noise introduced by cosmic shear. This low level of shape noise leads to stronger relative noise contributions from cosmic shear compared to the CFHTLenS analysis.

Table 2. Weak lensing results using the CFHTLenS data – Column 1: split between red and blue galaxies. Column 2: stellar mass range. Columns 3 and 4: radius r_{200c} and mass M_{200c} as estimated from the isotropic component of the shear signal from the fields passing the systematics tests ('pass fields'). Columns 5 and 6: aligned ellipticity ratio f_h and reduced χ^2 for the f_h fit from the analysis of the 'pass fields'. Columns 7 and 8: aligned ellipticity ratio f_h and reduced χ^2 for the f_h fit from the analysis of all fields.

Colour	Stellar mass $[M_\odot]$	r_{200c} [kpc/h_{70}]	M_{200c} [$10^{11}\,M_\odot/h_{70}$]	Pass fields f_h	Pass fields χ^2/d.o.f.	All fields f_h	All fields χ^2/d.o.f.
Red	$10 < \log_{10} M_* < 10.5$	170	8.6 ± 1.7	$-0.11^{+0.73}_{-0.73}$	9.6/7	$-0.31^{+0.59}_{-0.60}$	7.8/7
Red	$10.5 < \log_{10} M_* < 11$	253	28.2 ± 2.9	$0.01^{+0.35}_{-0.35}$	9.5/10	$-0.20^{+0.29}_{-0.29}$	8.8/10
Red	$\log_{10} M_* > 11$	377	93.3 ± 10.3	$-0.09^{+0.38}_{-0.38}$	11.3/12	$-0.01^{+0.33}_{-0.33}$	14.0/12
Red	$\log_{10} M_* > 10$			$-0.04^{+0.25}_{-0.25}$	30.5/31	$-0.17^{+0.21}_{-0.21}$	30.6/31
Blue	$9.5 < \log_{10} M_* < 10$	128	3.7 ± 0.8	$1.27^{+0.88}_{-0.81}$	7.5/5	$0.89^{+0.75}_{-0.70}$	11.2/6
Blue	$10 < \log_{10} M_* < 10.5$	191	12.1 ± 2.0	$0.18^{+0.51}_{-0.50}$	2.8/8	$0.35^{+0.49}_{-0.49}$	3.8/8
Blue	$\log_{10} M_* > 10.5$	234	22.2 ± 4.4	$1.11^{+0.67}_{-0.64}$	7.3/9	$0.51^{+0.52}_{-0.51}$	9.9/9
Blue	$\log_{10} M_* > 9.5$			$0.69^{+0.37}_{-0.36}$	20.5/24	$0.56^{+0.34}_{-0.33}$	24.8/25

This increases the noise correlations between different radial bins. While they can be substantial for the isotropic signal $\Delta\Sigma$ for some of the lens bins with 5 percent $< |\langle \mathrm{cor}_{i,j}\rangle_{i>j}| <$ 45 percent, they are generally small for the anisotropic signal $(f - f_{45})\Delta\Sigma$ with $|\langle \mathrm{cor}_{i,j}\rangle_{i>j}| \lesssim 4$ percent. Noise in the latter dominates the uncertainties in the f_h constraints. We therefore expect that the net impact of the noise correlations on our constraints is negligible. As a consistency check we also repeat the analysis of the simulated data with more realistic shape noise ($\sigma_e = 0.25$). Here we find consistent results, but the increased statistical uncertainty makes it impossible to detect the signal for some of the weakly aligned lens models.

4.2 Mock lens galaxies

For the foreground lenses we make use of galaxy shapes computed by Joachimi et al. (2013a, hereafter J13a) and Joachimi et al. (2013b, hereafter J13b). Following Bett et al. (2007), haloes and their member candidate particles are first identified by a friends-of-friends algorithm (Davis et al. 1985). In a second step, merger-tree data is used to remove particles belonging to substructures that are only temporarily in the halo vicinity. Halo shapes are then estimated via the full quadrupole tensor of the halo's matter distribution that remains after removal of these transients. This information is complemented with semi-analytic galaxy evolution models (Bower et al. 2006) and a classification of galaxy morphologies into early and late types via the bulge-to-total ratio of the rest-frame *K*-band luminosity (Parry, Eke & Frenk 2009). They also separate galaxies into centrals (galaxies in the most massive substructure of a halo) and satellites. Here we only use foreground galaxies classified as centrals because J13a and J13b had to assign simplistic galaxy shapes to the satellites given that their dark matter haloes were poorly resolved. Also, we only keep those foreground galaxies with a sufficient particle number for robust shape estimation, see J13a. For the centrals J13a and J13b assign shapes adopting the scheme of Heymans et al. (2006b). Here, late-type disc-dominated galaxies are aligned such that their spin vector is parallel to the angular momentum vector of their host dark matter halo. These shapes are then projected on to the plane of the sky. For early type galaxies, it is assumed that the shapes of the galaxies follow the shapes of their dark matter haloes. For this J13a project the ellipsoid given by the eigenvectors and eigenvalues of the inertia tensor for each halo on to the plane of the sky and use the resulting ellipse as the shape of the galaxy.

We additionally consider galaxy ellipticities that are misaligned with respect to their host dark matter halo as detailed in J13b. For early type galaxies the misalignment angles were drawn from a Gaussian distribution with a scatter of 35° as estimated by Okumura et al. (2009) from the distribution of satellites around LRGs in SDSS. For late-type galaxies J13b employ a misalignment distribution based on a fitting function that Bett (2012) determined using a compilation of simulated haloes with baryons and galaxy formation physics (Bett et al. 2010; Deason et al. 2011; Crain et al. 2009; Okamoto et al. 2005).

Similarly to the analysis of the CFHTLenS data, we select lens galaxies in the redshift range $0.2 < z_l < 0.6$ split into two redshift slices (which we analyse separately because of better S/N compared to CFHTLenS) and stellar mass bins, see Table 3 for details.

4.3 Results

We summarize the main results of the analysis based on the Millennium Simulation in Table 3, listing estimated halo masses, as well as f_h constraints for both aligned and misaligned galaxy shape models, each with and without foreground cosmic shear applied. For this analysis, we use modified ΛCDM cosmological parameters for the evaluation of angular diameter distances, matching the input to the Millennium Simulation, with $\Omega_m = 0.25$, $\Omega_\Lambda = 0.75$, $H_0 = 73h_{73}$ km s^{-1} Mpc^{-1}.

4.3.1 Halo masses

In the CFHTLenS analysis, we use stellar mass as proxy for halo mass. For the analysis of the Millennium Simulation, we again split the lenses into stellar mass bins. However, these stellar mass estimates are based on semi-analytic galaxy evolution models (Bower et al. 2006) which have some uncertainty (e.g. Kim et al. 2009; Saghiha et al. 2012). For a direct comparison of the results from CFHTLenS and the simulation it is more relevant that the included bins roughly span the same range in halo mass. Here, we note that the halo mass estimates inferred from the isotropic shear signal agree reasonably well for the late-type (blue) lenses, whereas the early-type (red) lenses yield higher halo masses in a given stellar mass bin

Table 3. Weak lensing results using the mock data based on the Millennium Simulation, both for the analysis with and without foreground cosmic shear (c.s.) applied. Summary of the results from the analysis of the Millennium Simulation – Column 1: split between early and late types. Column 2: stellar mass range. Column 3: minimum lens redshift. Column 4: maximum lens redshift. Column 5: ellipticity dispersion of the selected lenses with $0.05 < |e_g| < 0.95$ combining both components. Columns 6 and 7: radius r_{200c} and mass M_{200c} as estimated from the isotropic component of the shear signal for the aligned lens models with cosmic shear (very small differences for the other models). Columns 8 and 9: aligned ellipticity ratio f_h for aligned lens models (models `Est` and `Sa1` from J13b) with and without foreground cosmic shear applied, respectively. Columns 10 and 11: aligned ellipticity ratio f_h for misaligned lens models (models `Ema` and `Sma` from J13b) with and without foreground cosmic shear applied, respectively.

Type	Stellar mass	$z_{l,\,min}$	$z_{l,\,max}$	σ_e	r_{200c} [kpc/h_{73}]	M_{200c} [10^{11} M$_\odot/h_{73}$]	f_h (aligned) with c.s.	f_h (aligned) without c.s.	f_h (misaligned) with c.s.	f_h (misaligned) without c.s.
Early	$9.5 < \log_{10} M_* < 10$	0.2	0.4	0.19	168	7.84 ± 0.03	$0.504^{+0.027}_{-0.025}$	$0.511^{+0.026}_{-0.026}$	$0.203^{+0.027}_{-0.026}$	$0.219^{+0.028}_{-0.026}$
Early	$10 < \log_{10} M_* < 10.5$	0.2	0.4	0.19	226	18.97 ± 0.06	$0.635^{+0.015}_{-0.015}$	$0.644^{+0.015}_{-0.015}$	$0.306^{+0.015}_{-0.014}$	$0.298^{+0.016}_{-0.014}$
Early	$10.5 < \log_{10} M_* < 11$	0.2	0.4	0.19	375	86.19 ± 0.25	$0.759^{+0.009}_{-0.009}$	$0.772^{+0.010}_{-0.008}$	$0.373^{+0.010}_{-0.008}$	$0.376^{+0.010}_{-0.008}$
Early	$11 < \log_{10} M_* < 11.5$	0.2	0.4	0.21	563	291.14 ± 1.69	$0.846^{+0.012}_{-0.011}$	$0.863^{+0.011}_{-0.011}$	$0.402^{+0.011}_{-0.010}$	$0.407^{+0.012}_{-0.010}$
Early	$9.5 < \log_{10} M_* < 11.5$	0.2	0.4	0.19			$0.715^{+0.007}_{-0.006}$	$0.726^{+0.007}_{-0.006}$	$0.344^{+0.007}_{-0.006}$	$0.346^{+0.007}_{-0.006}$
Early	$9.5 < \log_{10} M_* < 10$	0.4	0.6	0.20	156	7.56 ± 0.03	$0.407^{+0.021}_{-0.021}$	$0.463^{+0.022}_{-0.020}$	$0.144^{+0.022}_{-0.021}$	$0.209^{+0.022}_{-0.021}$
Early	$10 < \log_{10} M_* < 10.5$	0.4	0.6	0.20	213	19.15 ± 0.05	$0.501^{+0.013}_{-0.012}$	$0.535^{+0.013}_{-0.012}$	$0.232^{+0.013}_{-0.012}$	$0.259^{+0.012}_{-0.012}$
Early	$10.5 < \log_{10} M_* < 11$	0.4	0.6	0.21	351	86.34 ± 0.24	$0.660^{+0.009}_{-0.008}$	$0.679^{+0.009}_{-0.008}$	$0.299^{+0.009}_{-0.007}$	$0.332^{+0.009}_{-0.007}$
Early	$11 < \log_{10} M_* < 11.5$	0.4	0.6	0.22	502	251.61 ± 1.37	$0.805^{+0.012}_{-0.010}$	$0.827^{+0.011}_{-0.010}$	$0.359^{+0.011}_{-0.010}$	$0.379^{+0.011}_{-0.010}$
Early	$9.5 < \log_{10} M_* < 11.5$	0.4	0.6	0.21			$0.607^{+0.006}_{-0.006}$	$0.636^{+0.006}_{-0.006}$	$0.272^{+0.007}_{-0.005}$	$0.306^{+0.006}_{-0.005}$
Early	$9.5 < \log_{10} M_* < 11$	0.2	0.6	0.20			$0.616^{+0.006}_{-0.005}$	$0.637^{+0.006}_{-0.004}$	$0.285^{+0.006}_{-0.004}$	$0.307^{+0.005}_{-0.005}$
Early	$9.5 < \log_{10} M_* < 11.5$	0.2	0.6	0.20			$0.657^{+0.005}_{-0.004}$	$0.678^{+0.005}_{-0.004}$	$0.304^{+0.005}_{-0.004}$	$0.324^{+0.004}_{-0.004}$
Late	$9.5 < \log_{10} M_* < 10$	0.2	0.4	0.32	131	3.68 ± 0.01	$0.073^{+0.016}_{-0.016}$	$0.068^{+0.017}_{-0.015}$	$0.034^{+0.017}_{-0.016}$	$0.025^{+0.017}_{-0.016}$
Late	$10 < \log_{10} M_* < 10.5$	0.2	0.4	0.32	171	8.17 ± 0.03	$0.123^{+0.014}_{-0.013}$	$0.133^{+0.015}_{-0.013}$	$0.038^{+0.014}_{-0.014}$	$0.064^{+0.014}_{-0.014}$
Late	$10.5 < \log_{10} M_* < 11$	0.2	0.4	0.32	245	24.02 ± 0.10	$0.129^{+0.012}_{-0.011}$	$0.132^{+0.012}_{-0.011}$	$0.031^{+0.012}_{-0.012}$	$0.059^{+0.012}_{-0.012}$
Late	$9.5 < \log_{10} M_* < 11$	0.2	0.4	0.32			$0.108^{+0.009}_{-0.007}$	$0.111^{+0.009}_{-0.008}$	$0.034^{+0.009}_{-0.008}$	$0.049^{+0.009}_{-0.008}$
Late	$9.5 < \log_{10} M_* < 10$	0.4	0.6	0.32	124	3.82 ± 0.01	$0.041^{+0.014}_{-0.012}$	$0.068^{+0.013}_{-0.013}$	$0.007^{+0.014}_{-0.012}$	$0.013^{+0.014}_{-0.013}$
Late	$10 < \log_{10} M_* < 10.5$	0.4	0.6	0.32	163	8.68 ± 0.03	$0.101^{+0.012}_{-0.010}$	$0.122^{+0.012}_{-0.011}$	$0.022^{+0.012}_{-0.011}$	$0.031^{+0.012}_{-0.011}$
Late	$10.5 < \log_{10} M_* < 11$	0.4	0.6	0.32	230	24.38 ± 0.08	$0.115^{+0.010}_{-0.010}$	$0.128^{+0.010}_{-0.010}$	$0.029^{+0.011}_{-0.010}$	$0.037^{+0.011}_{-0.009}$
Late	$9.5 < \log_{10} M_* < 11$	0.4	0.6	0.32			$0.085^{+0.007}_{-0.007}$	$0.104^{+0.008}_{-0.006}$	$0.019^{+0.007}_{-0.006}$	$0.027^{+0.007}_{-0.007}$
Late	$9.5 < \log_{10} M_* < 11$	0.2	0.6	0.32			$0.095^{+0.005}_{-0.005}$	$0.107^{+0.006}_{-0.004}$	$0.025^{+0.006}_{-0.004}$	$0.036^{+0.006}_{-0.005}$

in the simulation. To roughly match the halo mass range when computing joint constraints on f_h from the simulation, we therefore remove the highest stellar mass bin ($11 < \log_{10} M_* < 11.5$) and instead include one additional, lower stellar mass bin ($9.5 < \log_{10} M_* < 10$). Given the only moderate dependence of f_h on mass (Table 3), this approximate matching is fully sufficient for our goal to provide model predictions.

4.3.2 *Shear profile plots*

We plot the isotropic and anisotropic shear profiles for an illustrative subset of the combinations of lens bins and shape models in Figs 6 and 7. From top to bottom, the panels show the isotropic profile $\Delta\Sigma(r)$ and the corresponding anisotropic profiles $(f - f_{45})\Delta\Sigma(r)$, $f\Delta\Sigma(r)$, and $-f_{45}\Delta\Sigma(r)$, both with (crosses) and without (circles) foreground cosmic shear applied to the lens ellipticities.[13]

Fig. 6 shows early-type lenses with high stellar mass $10.5 < \log_{10} M_* < 11$. Here, the left-hand and middle columns show the signal of lenses with aligned shape models at lower ($0.2 < z_l < 0.4$) and higher ($0.4 < z_l < 0.6$) redshift, respectively, illustrating the increasing cosmic shear contribution. The right-hand column shows the signal of the same lenses as the middle column, but now with misaligned shape models.

Fig. 7 shows the signal of other sets of lens galaxies at $0.2 < z_l < 0.4$ with aligned shape models, namely early types at lower stellar mass ($9.5 < \log_{10} M_* < 10$) in the left-hand column, as well as late types with high ($10.5 < \log_{10} M_* < 11$) and low ($9.5 < \log_{10} M_* < 10$) stellar mass in the middle and right-hand columns, respectively.

4.3.3 *Deviations in the isotropic shear profile*

We note that the isotropic $\Delta\Sigma$ profile falls below the NFW model at very small scales, especially for the lower mass haloes. This is caused by the force softening used in the Millennium Simulation and smoothing applied in the ray-tracing (Hilbert et al. 2009; Gillis et al. 2013). This is not problematic for our analysis given that we only include scales $r > 45\,\mathrm{kpc}/h_{73}$ in the fit. Also, the highest stellar mass bins for early types show a marginally steeper $\Delta\Sigma$ profile than the best-fitting NFW model (see Fig. 6). This could be caused by our use of the Duffy et al. (2008) mass–concentration

[13] The foreground cosmic shear is always applied to the sources, but it only has a net effect if it is applied to both lenses and sources.

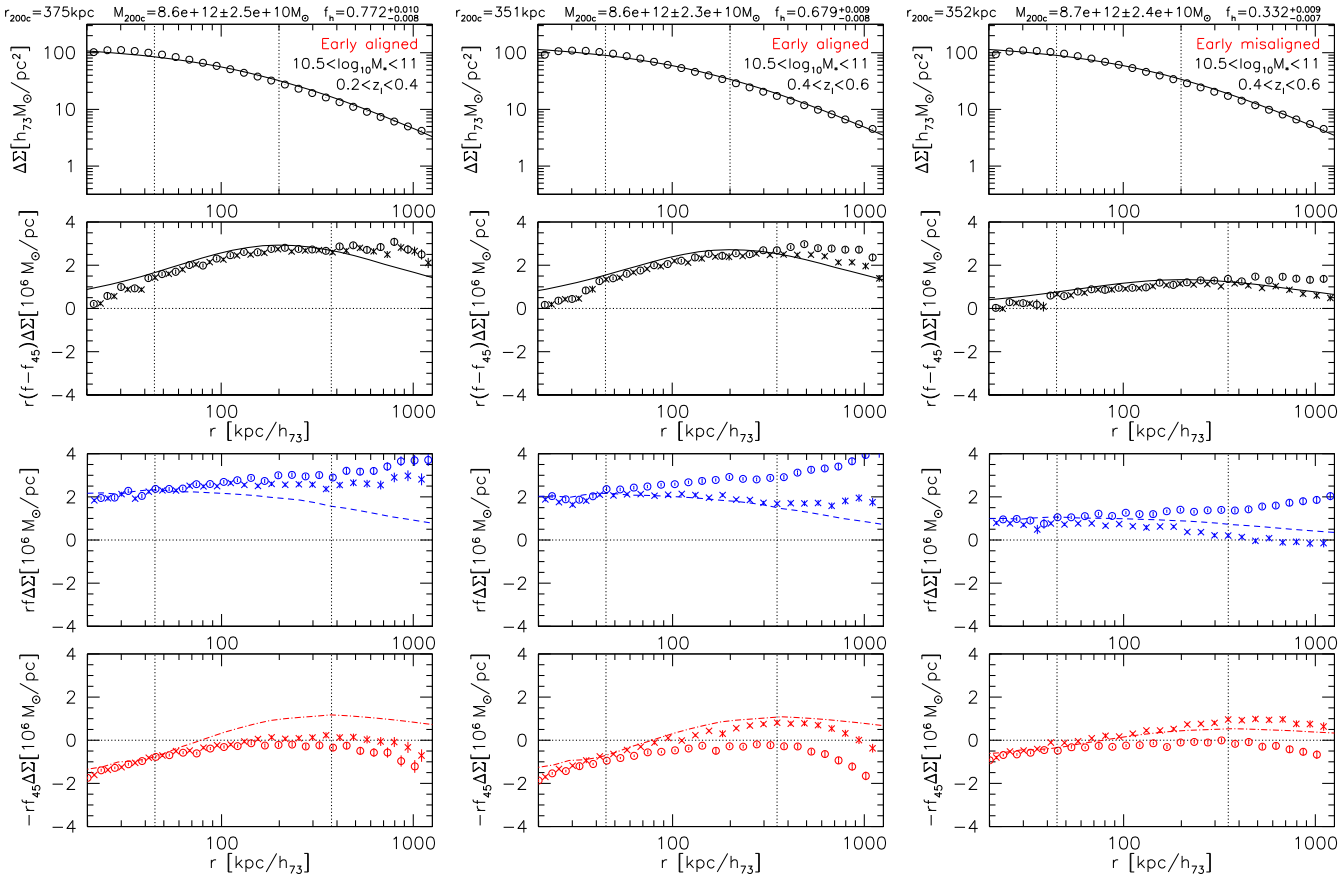

Figure 6. Analysis of the Millennium Simulation showing early-type foreground lens galaxies in stellar mass bin $10.5 < \log_{10} M_* < 11$: From top to bottom, we show the isotropic signal $\Delta\Sigma$ and the anisotropic signal components $(f - f_{45})\Delta\Sigma$, $f\Delta\Sigma$, and $-f_{45}\Delta\Sigma$, respectively. For the anisotropic signal components, the crosses (circles) correspond to the cases with (without) foreground cosmic shear applied, where the crosses are displayed with an offset of half a bin for better readability (note the scaling by r for better readability). The left-hand column corresponds to aligned shape models and lens redshift slice $0.2 < z_l < 0.4$. The middle column also shows aligned shape models but higher lens redshifts $0.4 < z_l < 0.6$, illustrating the effect of an increasing cosmic shear contribution. The right-hand column corresponds to the same lens galaxies as the middle column, but now with misaligned shape models, illustrating the resulting suppression of the anisotropic signal. The curves indicate the model predictions for the best-fitting f_h and best-fitting isotropic model. f_h is determined from the ratio of $(f - f_{45})\Delta\Sigma$ and $\Delta\Sigma$ for the case without cosmic shear, fitted within the range indicated by the vertical dotted lines.

relation, which was derived using N-body simulations with a significantly different input cosmology than the one used in the Millennium Simulation ($\sigma_8 = 0.796$ versus $\sigma_8 = 0.9$), see e.g. Ludlow et al. (2014) regarding the cosmology dependence of the mass–concentration relation. Since we estimate f_h directly from the ratio of the measured $(f - f_{45})\Delta\Sigma$ and $\Delta\Sigma$, the impact of these deviations is negligible for our analysis, especially compared to the statistical uncertainties from CFHTLenS. However, as a result the model curve for $(f - f_{45})\Delta\Sigma$, which is computed from the model for $\Delta\Sigma$ and the best-fitting f_h, is slightly biased high compared to the data in Fig. 6.

4.3.4 *Influence of cosmic shear*

In the two bottom rows of panels in Figs. 6 and 7 we show the anisotropic components $f\Delta\Sigma$ and $-f_{45}\Delta\Sigma$, which are decreased and increased, respectively, due to the cosmic shear contribution. Here the relative effect is stronger towards larger radii, higher redshifts, lower halo masses, and lower f_h. In contrast, $(f - f_{45})\Delta\Sigma$ is only weakly affected by the cosmic shear contribution within the fitted range ($45\,\mathrm{kpc}/h_{70} < r < r_{200c}$) as visible in the second row of panels, but we note that it is decreased at larger radii compared to the case without cosmic shear. This is a result of the non-vanishing ξ_- at these scales (see Section 2.1). We stress that our approach using the M06 formalism and restricting the fit range below r_{200c} efficiently suppresses the impact of cosmic shear. As visible in Table 3, the remaining net effect is $\Delta f_h \lesssim 0.02$ averaged over our redshift range, which is an order of magnitude smaller than current observational uncertainties.

4.3.5 *Indications of large-scale structure shape–shear correlations*

We note that the anisotropic shear signal shows deviations from the simple elliptical NFW model even in the case that no foreground cosmic shear is applied to the lens ellipticities, as best visible for the early-type galaxies in Figs. 6 and 7. For the early-type galaxies the measured signal is increased for $f\Delta\Sigma$ and decreased for $-f_{45}\Delta\Sigma$ compared to the model that assumes an isolated single elliptical NFW halo. This trend is the strongest at large radii (for the scaling by r shown in the plot), but especially for the lower mass haloes it is visible down to small radii (left-hand column of Fig. 7). This

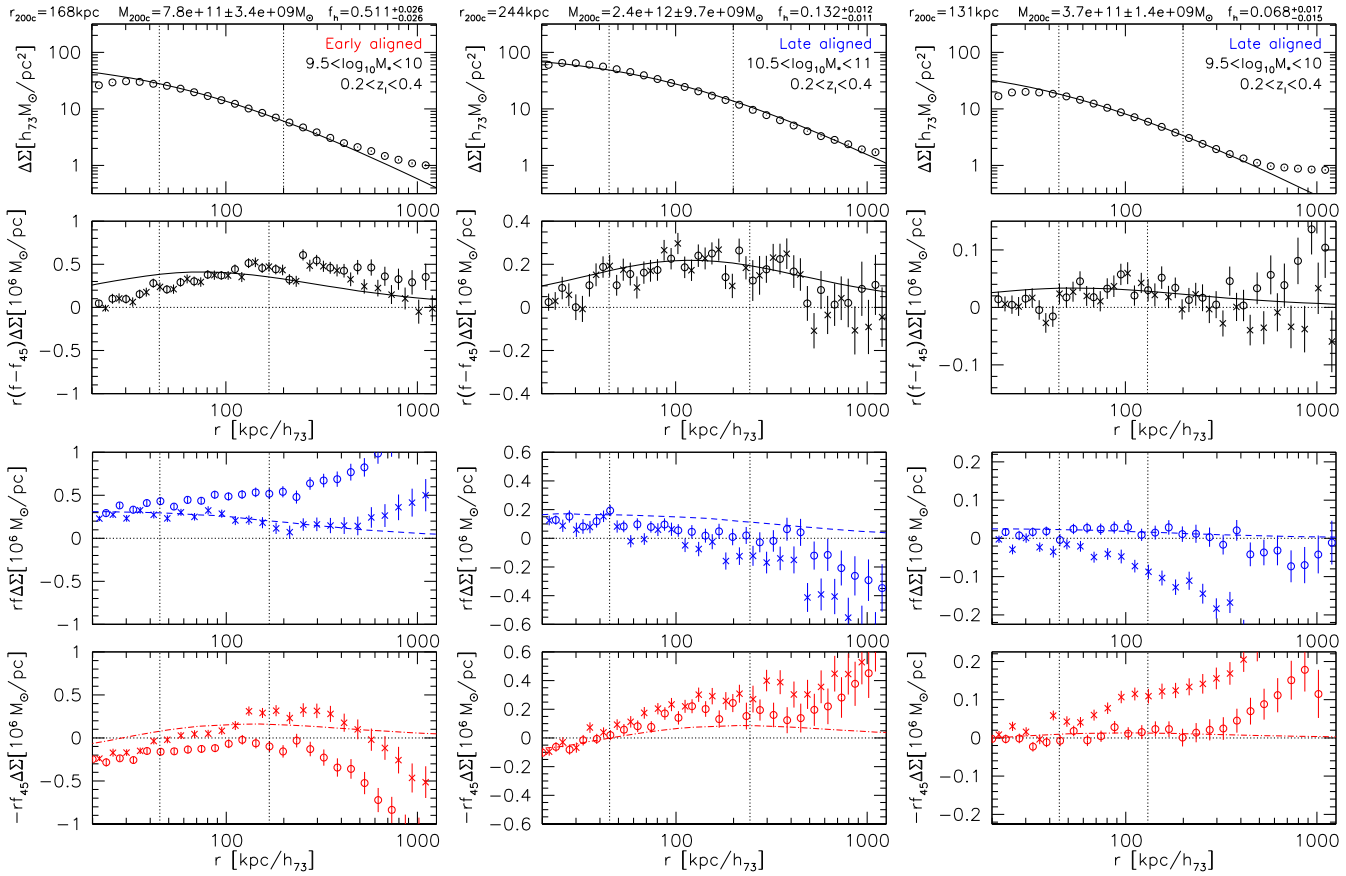

Figure 7. Analysis of the Millennium Simulation showing lenses at $0.2 < z_l < 0.4$ with aligned shape models: the left-hand column shows early-type galaxies with stellar mass $9.5 < \log_{10}M_* < 10$. The middle column corresponds to late-type galaxies in stellar mass bin $10.5 < \log_{10}M_* < 11$. The right-hand column also shows the signal of late-type galaxies, but with lower stellar masses $9.5 < \log_{10}M_* < 10$. For further details see the caption of Fig. 6.

has the opposite effect compared to the foreground cosmic shear which aligns the lens and the source. In fact, both effects actually cancel fairly well for the middle column in Fig. 6. Accordingly, this means that the ellipticities of the foreground lenses and the background sources become anti-aligned because of this effect. This is precisely the signature of shape–shear correlations, which are one of the intrinsic alignment contaminants to cosmic shear (e.g. Hirata & Seljak 2004; Joachimi et al. 2011; Heymans et al. 2013), and which were studied using the same simulations in J13b. They are caused by alignments of the foreground galaxies with their surrounding large-scale structure, which lenses the background source galaxies. Note that the halo ellipticity signal we want to extract contributes to shape–shear correlations itself, but an additional contribution comes from the surrounding large-scale structure. We suspect that the additional signal we are detecting here in the context of halo shape measurements is caused by this large-scale structure contribution.

Note that this effect appears to be weaker for the late-type lenses, in agreement with observational constraints (Mandelbaum et al. 2011), but also with the J13b intrinsic alignments analysis of these simulations. For late-type galaxies, the strongest deviations from the single NFW models are visible for the highest stellar mass bin in the middle column of Fig. 7. Here they appear to have the same sign as cosmic shear (alignment of lenses and sources), but in absolute terms the effect is weaker and the constraints are more noisy than for the early types.

The observed profiles for $f\Delta\Sigma$, $-f_{45}\Delta\Sigma$, and $(f - f_{45})\Delta\Sigma$ experience a similar relative suppression when misaligned lenses are studied compared to aligned lenses, if foreground cosmic shear is not applied (compare the middle and the right-hand column of Fig. 6). This is expected given that random misalignment of lens galaxies suppresses both the halo shape signature and the additional signal from shape–shear correlations caused by alignments of the lens galaxies with their large-scale environment. In contrast, the application of foreground cosmic shear introduces additional additive signal which is the same for aligned and misaligned lens models.

To further test our hypothesis that the extra signal is caused by shape–shear correlations from the large-scale environment, we further investigate the signal of the aligned early-type galaxies at $0.4 < z_l < 0.6$ with $10.5 < \log_{10}M_* < 11$. For these galaxies, the plots in the middle column of Fig. 6 suggest that the contributions from cosmic shear and shape–shear correlations cancel approximately. For these lenses and their surrounding background sources, we compare the two-point correlation functions

$$\xi_\pm^{\rm GI}(r) = \langle e_{\rm l,t}^{\rm int}\gamma_{\rm s,t} \pm e_{\rm l,\times}^{\rm int}\gamma_{\rm s,\times}\rangle(r) \qquad (25)$$

between the (not-lensed) intrinsic lens ellipticities $e_{\rm l}^{\rm int}$ and the background shears (shape–shear signal), versus the corresponding cosmic shear correlation functions

$$\xi_\pm^{\rm GG}(r) = \langle \gamma_{\rm l,t}\gamma_{\rm s,t} \pm \gamma_{\rm l,\times}\gamma_{\rm s,\times}\rangle(r)\,. \qquad (26)$$

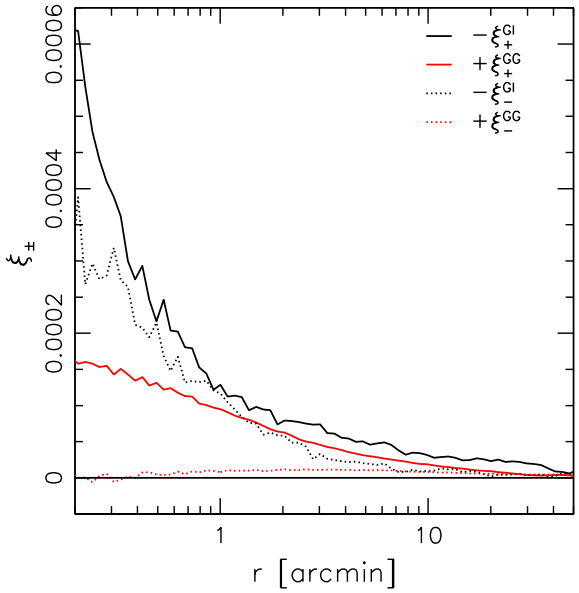

Figure 8. Shear–shear and shape–shear correlation functions $\xi_\pm^{GG}$ and $-\xi_\pm^{GI}$ for the aligned early-type galaxies in the Millennium Simulation at $0.4 < z_l < 0.6$ with $10.5 < \log_{10}M_* < 11$. For these lenses r_{200c} equals 0.98 arcmin.

As shown in Fig. 8, ξ_+^{GI} and ξ_+^{GG} are of roughly comparable amplitude (note the opposite sign) over a wide range in scale ($r \gtrsim 0.6$ arcmin). This is consistent with the interpretation that the influence of cosmic shear and the influence of the shape–shear correlations on the halo shape measurement cancel approximately. Note however that $\xi_\pm^{GI}$ mixes contributions from both the halo shape signal (primarily at small r) and the shape–shear correlations from the large-scale environment (affecting also larger r). Therefore, we do not attempt to interpret Fig. 8 more quantitatively.

As demonstrated in Section 4.3.4, halo shape estimates based on $(f - f_{45})\Delta\Sigma$ are insensitive to extra alignment from cosmic shear if a limited radial range is included in the fit as done in our analysis. Given that the radial dependence of the measured $(f - f_{45})\Delta\Sigma$ signal is reasonably well described by the model prediction within the fit range for most of our lens bins, we suspect that this formalism also provides an approximate correction for the extra alignment caused by the surrounding large-scale structure. However, it is clear that this model of a single, isolated, elliptical NFW halo is only a very crude approximation of reality, and that some deviations due to the surrounding large-scale structure are still expected. For example, note the significant deviations from the best-fitting model also within the fit range in the left-hand column of Fig. 7. Nevertheless, as we perform a direct, consistent comparison of our CFHTLenS results to the constraints from the simulation, which ideally includes the same physical effects, the relative conclusions should not be affected substantially.

4.3.6 *Constraints on* f_h *for early-type galaxies*

We summarize the estimates for the aligned ellipticity ratio f_h for the different lens samples in Table 3. For early types, we generally measure larger f_h for more massive haloes. For example, the most massive low-z ellipticals yield $f_h = 0.863 \pm 0.011$ for the aligned lens galaxy models and no cosmic shear. For lower mass haloes, this value decreases, and we find $f_h = 0.616^{+0.006}_{-0.005}$ when applying cosmic shear and combining both redshift bins and the stellar mass range $9.5 < \log_{10}M_* < 11$, to best mimic our red galaxy sample in CFHTLenS.

This result is somewhat surprising: given that the projected lens shapes of early types are defined via the projected quadrupole tensor of the mass distribution in the simulation, we would naively expect to measure $f_h \simeq 1$ in all cases. We suggest three possible explanations for this, and we presume that all three may contribute in practice at different levels: First, the projected halo shapes are approximated via the quadrupole tensor of the mass distribution. However, the projected mass distributions will not have exactly elliptical shapes, and therefore deviate from the projected light distribution. Secondly, the haloes are embedded in a surrounding large-scale structure. Components of that large-scale structure that have a random orientation with respect to the orientation of the halo will add noise in the form of an on average spherical mass distribution, reducing f_h. Also the transient subhaloes, which have been removed (see Section 4.2), contribute to this. Finally, the surrounding large-scale structure may have a component that is aligned with respect to the halo orientation, causing the extra signal discussed in Section 4.3.5. While we expect that our analysis using $(f - f_{45})\Delta\Sigma$ partially separates this component from the signal of the halo, there may be some residual effect impacting the f_h constraints. A hint for this is visible in the left-hand column of Fig. 7, where the model fits the measured $(f - f_{45})\Delta\Sigma$ relatively poorly. We note that the second and third effect are likely more pronounced for less massive haloes for which the surrounding large-scale structure has a larger relative impact, in agreement with the trend observed.

For the misaligned lens models f_h generally decreases as expected, and we find $f_h = 0.285^{+0.006}_{-0.004}$ for the combined lens sample.

4.3.7 *Constraints on* f_h *for late-type galaxies*

For the late-type galaxies the recovered values of f_h are generally small, with $f_h = 0.095 \pm 0.005$ in the case of aligned models and $f_h = 0.025^{+0.006}_{-0.004}$ for misaligned models, combining all lens samples and applying cosmic shear. This indicates that even if the angular momentum vector of each dark matter halo was perfectly aligned with the spin axis of its disc galaxy, the halo shape signal would be largely washed out due to misalignment between the mass distribution and the angular momentum vector of the halo. Once galaxy misalignments are included, the net signal is so small that it should remain undetected even with much larger surveys than CFHTLenS. Despite this generally low signal, there is a trend that f_h increases in the simulated data for more massive haloes.

4.3.8 *Accounting for the differences in the ellipticity dispersions between CFHTLenS and the simulation*

We can directly compare our constraints on f_h from the Millennium Simulation to those from CFHTLenS if we assume that our procedure to assign galaxy ellipticities to the haloes in the simulation is adequate. However, if we compare the ellipticity dispersions σ_e (including both ellipticity components) of the selected lenses between CFHTLenS (Table 1) and the simulation (Table 3), we find that the average dispersions are somewhat higher in CFHTLenS, with $\sigma_e^{\rm CFHTLenS} = 0.29\,(0.35)$ for red (blue) lenses, compared to $\sigma_e^{\rm simulation} = 0.20\,(0.32)$ for the early (late) types in the Millennium Simulation. Hence, the simulation appears to deliver on average too round lenses, especially for early types. As a first-order correction

for this discrepancy one could increase the lens ellipticities in the simulation by a factor

$$s = \frac{\sigma_{\rm e}^{\rm CFHTLenS}}{\sigma_{\rm e}^{\rm simulation}} \simeq 1.46\,(1.10) \qquad (27)$$

if one assumes that the early- (late-) type galaxies in the simulation resemble the red (blue) galaxies in CFHTLenS. We choose to not directly rescale the ellipticities, but to keep the analysis comparable to earlier studies using these mock catalogues (Joachimi et al. 2013a,b). From the definition of $f_{\rm h}$ (see Eq. 11) it is directly evident that such a linear increase of the lens ellipticities $e_{\rm g}$ will reduce $f_{\rm h}$ by the same factor given that the shear signal (and hence $e_{\rm h}$) in the simulation is unchanged. Accordingly, when conducting a comparison in Section 5 that assumes that the red (blue) CFHTLenS sample corresponds to the early- (late-) type sample in the simulation, we will reduce the $f_{\rm h}$ estimate from the simulation by a factor s.

We also considered alternative approaches to compute scale factors s for the approximate matching of the ellipticity distributions between CFHTLenS and the simulation, such as the ratios $\langle|e_{\rm g}|\rangle^{\rm CFHTLenS}/\langle|e_{\rm g}|\rangle^{\rm simulation} = 1.39\,(1.09)$ or $(\langle|e_{\rm g}|^2\rangle/\langle|e_{\rm g}|\rangle)^{\rm CFHTLenS}/(\langle|e_{\rm g}|^2\rangle/\langle|e_{\rm g}|\rangle)^{\rm simulation} = 1.52$ (1.11), where the latter is equivalent to matching the $\langle|e_{\rm g}|\rangle$ with an extra weighting by $|e_{\rm g}|$ as employed in equations (15) and (16). The resulting differences of $\pm$5percent ($\pm$1percent) compared to equation (27) are small, especially compared to the statistical uncertainties from CFHTLenS. Also note that we do not need to correct the measured lens ellipticity dispersions in CFHTLenS for measurement noise given the high signal-to-noise ratio of all lenses in our analysis[7].

5 DISCUSSION AND CONCLUSIONS

Using CFHTLenS observational data we have obtained weak lensing constraints on $f_{\rm h}$, the ratio between the aligned projected ellipticity components of galaxy-scale matter haloes and their galaxies. In addition, we have used simulated data sets based on the Millennium Simulation to test the methodology and obtain an estimate for the expected signal given current alignment models for galaxies and their dark matter haloes.

In this analysis, we make use of the formalism introduced by M06 to correct for additional alignments of lenses and sources, e.g. due to residual shape systematics or cosmic shear. We demonstrate that this method removes a simplistic, constant alignment. In addition, we demonstrate that a realistic cosmic shear field, as present in the Millennium Simulation, is well removed for the fit range we employ, leaving residuals $\Delta f_{\rm h} \lesssim 0.02$ for our lens redshift range ($0.2 < z_{\rm l} < 0.6$), which is an order of magnitude smaller than current statistical uncertainties from CFHTLenS. We demonstrate that a more simplistic estimator that only considers the azimuthal variation in the tangential shear component is highly biased (see e.g. the third panel in the right-hand column of Fig. 7) as previously pointed out by Brainerd (2010) and Howell & Brainerd (2010).

From the CFHTLenS data, we estimate $f_{\rm h} = -0.04 \pm 0.25$ for red lenses and $f_{\rm h} = 0.69^{+0.37}_{-0.36}$ for blue lenses combining all stellar mass bins with $\log_{10}M_* > 10$ ($\log_{10}M_* > 9.5$) for the red (blue) lenses. The colour separation is done via the photometric type from BPZ, which we use as a proxy for the separation into early- and late-type galaxies. As discussed below, these values are broadly consistent with theoretical models.

In our analysis of the Millennium Simulation, we use different models for the alignment of galaxies with their dark matter haloes for early- and late-type galaxies. For late-type galaxies, the analysis assumes that the spin vectors of disc galaxies are aligned with the angular momentum vectors of their dark matter haloes. In the case of perfect alignment, we find $f_{\rm h} = 0.095 \pm 0.005$ from the Millennium Simulation, which reduces to $f_{\rm h} = 0.025^{+0.006}_{-0.004}$ for models which assume the misalignment distribution from Bett (2012). This distribution is based on a compilation of results from simulations that include baryons and galaxy formation physics (Okamoto et al. 2005; Crain et al. 2009; Bett et al. 2010; Deason et al. 2011). If we rescale these results as discussed in Section 4.3.8 to account for the differences in the lens ellipticity dispersions in CFHTLenS versus the simulation, these values change to $f_{\rm h} = 0.086 \pm 0.005$ for the aligned models and $f_{\rm h} = 0.023^{+0.005}_{-0.004}$ for the misaligned models. Based on the simulation we do not expect to detect a significant signal for late-type galaxies in CFHTLenS. Our CFHTLenS constraint for blue galaxies is higher than the scaled prediction for the aligned models by 1.7σ, and higher by 1.9σ compared to the scaled prediction for the misaligned models.

For early-type galaxies, the analysis of the simulation assumes that the lens ellipticities follow the ellipticity of the projected inertia tensor of the halo mass distribution. Hence, the projected galaxy shapes follow approximately the projected dark matter shapes. In the case of no misalignment, we estimate $f_{\rm h} = 0.616^{+0.006}_{-0.005}$ from the simulation when matching the measured halo mass range of the CFHTLenS constraints approximately. When applying a Gaussian misalignment distribution with an rms scatter of 35° (as suggested by the distribution of satellites around LRGs in SDSS; see Okumura et al. 2009), we estimate a value of $f_{\rm h} = 0.285^{+0.006}_{-0.004}$. If we rescale these results as discussed in Section 4.3.8 to account for the differences in the lens ellipticity dispersions in CFHTLenS versus the simulation, the values change to $f_{\rm h} = 0.422^{+0.004}_{-0.003}$ for the aligned models and $f_{\rm h} = 0.195^{+0.004}_{-0.003}$ for the misaligned models. Assuming that the red CFHTLenS galaxies directly correspond to the simulated early-type galaxies would mean that our CFHTLenS constraints are lower than the rescaled aligned prediction by 1.8σ, and lower by 0.9σ compared to the rescaled misaligned prediction. Hence, they are poorly described by the perfectly aligned model but fully consistent with the misaligned model.

It is interesting to compare our constraints to the results of recent hydrodynamical simulations. Tenneti et al. (2014) find a mean 3D misalignment angle at $z = 0.3$ of 25.°20 for a halo mass bin $10^{11.5}\,h^{-1}\,{\rm M}_\odot < M < 10^{13}\,h^{-1}\,{\rm M}_\odot$ which most closely matches the mass range of our red galaxies, but this increases to 33.°47 for lower halo masses $10^{10}\,h^{-1}\,{\rm M}_\odot < M < 10^{11.5}\,h^{-1}\,{\rm M}_\odot$. The misalignment distribution estimated by Okumura et al. (2009) and assumed in our simulated analysis (rms scatter of 35°) would correspond to a similar *mean* value of ∼28° (Tenneti et al. 2014). Thus, our assumed misalignment model approximately matches the results of this hydrodynamical simulation. However, for the direct comparison between observations and simulations there are additional relevant effects to be considered: for example, baryons appear to make the inner halo more spherical (Bryan et al. 2013). In addition, subhaloes are found to be rounder than haloes (Kuhlen, Diemand & Madau 2007; Tenneti et al. 2014). Accordingly, as our analysis of early-type galaxies in the simulation uses central haloes only, and given that it does not include baryons, we expect that our simulation should somewhat overpredict $f_{\rm h}$. A further complication for the comparison arises from the observation that numerical simulations of galaxy formation suggest that dark matter halo shapes are misaligned at different radii (e.g. Schneider, Frenk & Cole 2012; Wang et al. 2014).

A number of previous studies have attempted to constrain halo ellipticity with weak lensing observationally. Two previous studies

were able to split the lens sample into red and blue galaxies as done in our study: M06 find $f_{\rm h} = 0.60 \pm 0.38$ for red and $f_{\rm h} = -1.4^{+1.7}_{-2.0}$ for blue lenses, assuming an elliptical NFW mass profile and employing data from the SDSS. Using data from the RCS2 and employing the same formalism as M06, van Uitert et al. (2012) find $f_{\rm h} = 0.20^{+1.34}_{-1.31}$ for red lenses and $f_{\rm h} = -2.17^{+1.97}_{-2.03}$ for blue lenses when assuming an elliptical NFW mass profile and using linear weighting with the lens ellipticity as done in our study. While our error bars appear to be substantially tighter than those of these two studies, we note that our analysis of simulated data suggests a sign error in the numerical model prediction computed by M06 for f_{45}, which was also employed by van Uitert et al. (2012). This sign error has likely biased their derived constraints. With the corrected sign the predicted signal for $(f - f_{45})\Delta\Sigma$ is higher at a given $f_{\rm h}$ over the entire radial fit range and does not drop as quickly towards large r (see Fig. 1). Accordingly, this correction leads to significantly tighter constraints on $f_{\rm h}$.

Hoekstra et al. (2004) and Parker et al. (2007) use single-band data from RCS and early CFHTLS observations, respectively, to constrain halo ellipticity without subdivision into red and blue galaxies. They do not correct for systematic alignment between lenses and sources as introduced by M06. Hoekstra et al. (2004) conduct a maximum likelihood analysis assuming elliptical, truncated isothermal sphere (TIS) models from which they find $f_{\rm h} = 0.77^{+0.18}_{-0.21}$. Parker et al. (2007) compute the ratio of the shears measured in quadrants along the lens minor and major axes, for which they find a tentative signal 0.76 ± 0.10 when averaged out to 70 arcsec. There are differences in the anisotropic shear fields for NFW and TIS profiles (see M06), but none the less the $f_{\rm h}$ constraint from Hoekstra et al. (2004) may appear somewhat high even if their lens selection based on magnitude (without colours) would provide a perfect selection of early types, which is certainly not the case. The reason for this is that their formalism does not account for spurious alignment caused e.g. by foreground cosmic shear, which leads to a lower measured value of $f_{\rm h}$. Our analysis of the Millennium Simulation may provide a possible explanation for the high value of $f_{\rm h}$ measured by Hoekstra et al. (2004): As discussed in Section 4.3.5, we detect an excess signal in $f\Delta\Sigma$ for early-type lenses, which approximately corresponds to the signal probed by Hoekstra et al. (2004) and Parker et al. (2007). This excess signal has the opposite sign than the signal caused by cosmic shear (also visible in $-f_{45}\Delta\Sigma$). We interpret this signal as the impact of shape–shear intrinsic alignments, which are a major contaminant to cosmic shear measurements (e.g. Hirata & Seljak 2004; Joachimi et al. 2011; Heymans et al. 2013). They are caused by an alignment of foreground galaxies with their surrounding large-scale structure (as e.g. detected in the distribution of red galaxies; see Mandelbaum et al. 2006a; Li et al. 2013; Zhang et al. 2013), which also lenses the background sources. While the halo ellipticity signal contributes to small-scale shape–shear correlations itself (Bridle & Abdalla 2007), there appears to be an additional component generated by the large-scale structure the halo is embedded in. In other words, the assumed model of an isolated elliptical NFW halo is too simplistic. The net effect of this signal is a net anti-alignment (orthogonal alignment) of the ellipticities of foreground lenses and background sources. We expect that the formalism introduced by M06 and employed by us also provides a partial correction for this contaminant, but conclude that the most robust halo shape results can be obtained from the direct, relative comparison between observations and simulations that include this effect, as done in our study.

We note that our analysis of blue galaxies in CFHTLenS shows indications for the influence of cosmic shear on the (uncorrected) anisotropic shear components $f\Delta\Sigma$ (slightly negative signal in the third row of panels in Fig. 4) and $-f_{45}\Delta\Sigma$ (slightly positive signal in the fourth row of panels in Fig. 4). In contrast, we do not observe this trend for red galaxies (see Fig. 3). A likely explanation for this may be that the additional shape–shear signal discussed above appears to roughly cancel the cosmic shear contribution for our red galaxy sample. In contrast, the magnitude-selected lens samples from Hoekstra et al. (2004) and Parker et al. (2007) will likely be dominated by galaxies at lower redshift. Here, the shape–shear contribution will dominate given the smaller cosmic shear signal.

As discussed in Section 4.3.6, the influence of neighbouring large-scale structure is likely one of the main reasons why the analysis of the aligned early-type galaxies in the Millennium Simulation yields somewhat smaller $f_{\rm h}$ than the naive expectation of $f_{\rm h} \simeq 1$, in particular for the lower mass haloes.

The early-type lenses with the highest halo mass show the largest $f_{\rm h}$ in our simulation (see Table 3). In addition, more massive haloes are less spherical in simulations (e.g. Bailin & Steinmetz 2005; Despali, Giocoli & Tormen 2014). Furthermore, galaxies with more massive haloes are expected to be less misaligned (Tenneti et al. 2014). From all three effects, we expect that future studies with larger samples might have the best prospects for detecting halo ellipticity with weak lensing for very massive early-type galaxies. Very recently, Clampitt & Jain (2015) reported the detection of a significant halo shape signal for exactly such LRGs from SDSS, employing a new estimator from Adhikari, Chue & Dalal (2015). In the future, it will be interesting to test this estimator on large mock data sets, such as the data provided by the Millennium Simulation.

Weak lensing studies constraining halo ellipticity are not only interesting for a better understanding of the link between galaxies and their surrounding matter haloes, but have also been discussed as a possible test for theories of modified gravity such as MOND (Modified Newtonian Dynamics; Milgrom 1983), TeVeS (Scalar–Tensor–Vector theory; Bekenstein 2004), and MOG/STVG (Modified Gravity and Scalar–Tensor–Vector Gravity theory; Moffat 2006; Moffat & Toth 2009), for which lensing prescriptions have been developed (Mortlock & Turner 2001; Bekenstein 2004; Chiu, Ko & Tian 2006; Moffat & Toth 2009). The equivalent signals to halo shapes are discussed for isolated galaxies in Milgrom (2001) and Sellwood & Kosowsky (2002), predicting an isotropic shear signal towards large radii. Accordingly, a significant detection of halo ellipticity from weak lensing, which would be expected within ΛCDM for the analysis of early-type galaxies in upcoming experiments, could be interpreted as evidence against such theories of modified gravity. However, our analysis of the simulated data has shown that already within ΛCDM neighbouring structures have a considerable influence, which needs to be taken into account. Thus, better model predictions need to be developed also for theories of modified gravity that include both large-scale structure contributions and the influence of baryon physics.

The prospects for near-future improvements on halo shape constraints from weak lensing are relatively good: on the one hand, weak lensing surveys are improving rapidly in size. Surveys which are already underway include the Dark Energy Survey (DES; The Dark Energy Survey Collaboration 2005), the Hyper Suprime-Cam Subaru Strategic Program (HSC-SSP; Miyazaki et al. 2012), the Kilo Degree Survey (KiDS; de Jong et al. 2013), as well as the Panoramic Survey Telescope and Rapid Response System (PanSTARRS; Kaiser et al. 2010), and future programmes such as LSST (LSST Science Collaboration et al. 2009) and Euclid (Laureijs et al. 2011) will tighten parameter constraints even further.

On the other hand, the use of new estimators may also provide additional insight: Simon, Schneider & Kübler (2012) and Adhikari et al. (2015) suggest that the position angle dependence of the galaxy-shear–shear correlation function, which is one of the observables of galaxy–galaxy–galaxy lensing (Schneider & Watts 2005), may provide constraints on halo ellipticity independent of the orientation of the lens galaxy ellipticity. This measurement would be unaffected by misalignment, but is expected to have lower signal to noise. In addition, the measurement of higher order lensing ('flexion') may also provide additional sensitivity for constraining halo ellipticity (Er & Schneider 2011; Er & Bartelmann 2013).

ACKNOWLEDGEMENTS

We thank Rachel Mandelbaum and Peter Schneider for useful discussions and comments on this manuscript. We also thank Rachel Mandelbaum for making the tabulated predictions for $f_{\rm rel}$ and $f_{\rm rel,\,45}$ for an elliptical NFW profile available to us. We thank the referee for his or her comments, which have helped to improve the manuscript significantly.

This work is based on observations obtained with MegaPrime/MegaCam, a joint project of the CFHT and CEA/Irfu, at CFHT, which is operated by the National Research Council (NRC) of Canada, the Institut National des Sciences de l'Univers (INSU) at the Centre National de la Recherche Scientifique (CNRS) of France, and the University of Hawaii. This research used the facilities of the Canadian Astronomy Data Centre operated by the NRC of Canada with the support of the Canadian Space Agency. We thank the CFHT staff, in particular J.-C. Cuillandre and E. Magnier, for the observations, data processing, and continuous improvement of the instrument calibration. We also thank TERAPIX for quality assessment, and E. Bertin for developing some of the software used in this study. CFHTLenS data processing was made possible thanks to support from the Natural Sciences and Engineering Research Council of Canada (NSERC) and HPC specialist O. Toader. The early stages of the CFHTLenS project were made possible thanks to the European Commission's Marie Curie Research Training Network DUEL (MRTN-CT-2006-036133) and its support of CFHTLenS team members LF, HHi, and BR. This analysis makes use of data derived from the Millennium Simulation, which was carried out as part of the programme of the Virgo Consortium on the Regatta supercomputer of the Computing Centre of the Max-Planck-Society in Garching.

TS acknowledges support from NSF through grant AST-0444059-001, SAO through grant GO0-11147A, and NWO. SH acknowledges support by the National Science Foundation (NSF) grant number AST-0807458-002, and by the DFG cluster of excellence 'Origin and Structure of the Universe'. HHo acknowledges support from NWO VIDI grant number 639.042.814 and ERC FP7 grant 279396. PS receives support by the DFG through the project SI 1769/1-1. HHi is supported by the DFG Emmy Noether grant Hi 1495/2-1. PEB was supported by the Deutsche Forschungsgemeinschaft under the project SCHN 342/71 in the framework of the Priority Programme SPP-1177, and the Initiative and Networking Fund of the Helmholtz Association, contract HA-101 ('Physics at the Terascale'). LF acknowledges support from NSFC grant 11333001 & Shanghai Research grant 13JC1404400 of STCSM. BJ acknowledges support by an STFC Ernest Rutherford Fellowship, grant reference ST/J004421/1.

Author Contributions: All authors contributed to the development and writing of this paper. The authorship list reflects the lead authors of this paper (TS, SH, HHo, PS, EvU) followed by two alphabetical groups. The first alphabetical group includes key contributors to the science analysis and interpretation in this paper, the founding core team, and those whose long-term significant effort produced the final CFHTLenS data product. The second group covers members of the CFHTLenS team and collaborators who made a significant contribution to the project and/or this paper. The CFHTLenS collaboration was co-led by CH and LVW.

REFERENCES

Adhikari S., Chue C. Y. R., Dalal N., 2015, J. Cosmol. Astropart. Phys., 1, 9
Agustsson I., Brainerd T. G., 2010, ApJ, 709, 1321
Arnouts S., Cristiani S., Moscardini L., Matarrese S., Lucchin F., Fontana A., Giallongo E., 1999, MNRAS, 310, 540
Azzaro M., Patiri S. G., Prada F., Zentner A. R., 2007, MNRAS, 376, L43
Bailin J., Steinmetz M., 2005, ApJ, 627, 647
Bailin J. et al., 2005, ApJ, 627, L17
Bailin J., Power C., Norberg P., Zaritsky D., Gibson B. K., 2008, MNRAS, 390, 1133
Banerjee A., Jog C. J., 2008, ApJ, 685, 254
Bartelmann M., Schneider P., 2001, Phys. Rep., 340, 291
Bekenstein J. D., 2004, Phys. Rev. D, 70, 083509
Benítez N., 2000, ApJ, 536, 571
Benjamin J. et al., 2013, MNRAS, 431, 1547
Bertin E., Arnouts S., 1996, A&AS, 117, 393
Bett P., 2012, MNRAS, 420, 3303
Bett P., Eke V., Frenk C. S., Jenkins A., Helly J., Navarro J., 2007, MNRAS, 376, 215
Bett P., Eke V., Frenk C. S., Jenkins A., Okamoto T., 2010, MNRAS, 404, 1137
Bliss C. I., 1935a, Ann. Appl. Biol., 22, 134
Bliss C. I., 1935b, Ann. Appl. Biol., 22, 307
Bower R. G., Benson A. J., Malbon R., Helly J. C., Frenk C. S., Baugh C. M., Cole S., Lacey C. G., 2006, MNRAS, 370, 645
Brainerd T. G., 2005, ApJ, 628, L101
Brainerd T. G., 2010, ApJ, 713, 603
Brainerd T. G., Wright C. O., 2000, preprint (astro-ph/0006281)
Bridle S., Abdalla F. B., 2007, ApJ, 655, L1
Bruzual G., Charlot S., 2003, MNRAS, 344, 1000
Bryan S. E., Kay S. T., Duffy A. R., Schaye J., Dalla Vecchia C., Booth C. M., 2013, MNRAS, 429, 3316
Calzetti D., Armus L., Bohlin R. C., Kinney A. L., Koornneef J., Storchi-Bergmann T., 2000, ApJ, 533, 682
Chabrier G., 2003, PASP, 115, 763
Chiu M.-C., Ko C.-M., Tian Y., 2006, ApJ, 636, 565
Clampitt J., Jain B., 2015, preprint (arXiv:1506.03536)
Coe D., Benítez N., Sánchez S. F., Jee M., Bouwens R., Ford H., 2006, AJ, 132, 926
Corless V. L., King L. J., Clowe D., 2009, MNRAS, 393, 1235
Coupon J. et al., 2015, MNRAS, 449, 1352
Crain R. A. et al., 2009, MNRAS, 399, 1773
Davis M., Efstathiou G., Frenk C. S., White S. D. M., 1985, ApJ, 292, 371
de Jong J. T. A. et al., 2013, The Messenger, 154, 44
Deason A. J. et al., 2011, MNRAS, 415, 2607
Debattista V. P., van den Bosch F. C., Roškar R., Quinn T., Moore B., Cole D. R., 2015, MNRAS, 452, 4094
Despali G., Giocoli C., Tormen G., 2014, MNRAS, 443, 3208
Dong X. C., Lin W. P., Kang X., Ocean Wang Y., Dutton A. A., Macciò A. V., 2014, ApJ, 791, L33
Duffy A. R., Schaye J., Kay S. T., Dalla Vecchia C., 2008, MNRAS, 390, L64
Dutton A. A. et al., 2011, MNRAS, 417, 1621
Er X., Bartelmann M., 2013, MNRAS, 428, 103
Er X., Schneider P., 2011, A&A, 528, A52
Erben T. et al., 2009, A&A, 493, 1197
Erben T. et al., 2013, MNRAS, 433, 2545

Evans A. K. D., Bridle S., 2009, ApJ, 695, 1446
Faltenbacher A., Li C., Mao S., van den Bosch F. C., Yang X., Jing Y. P., Pasquali A., Mo H. J., 2007, ApJ, 662, L71
Faltenbacher A., Li C., White S. D. M., Jing Y.-P., Shu-DeMao, Wang J., 2009, Res. Astron. Astrophys., 9, 41
Fieller E. C., 1954, J. R. Stat. Soc. B, 16, 175
Ford J. et al., 2015, MNRAS, 447, 1304
Fu L. et al., 2014, MNRAS, 441, 2725
Gillis B. R., Hudson M. J., Hilbert S., Hartlap J., 2013, MNRAS, 429, 372
Harnois-Déraps J., Vafaei S., Van Waerbeke L., 2012, MNRAS, 426, 1262
Heymans C. et al., 2006a, MNRAS, 368, 1323
Heymans C., White M., Heavens A., Vale C., van Waerbeke L., 2006b, MNRAS, 371, 750
Heymans C. et al., 2012, MNRAS, 427, 146
Heymans C. et al., 2013, MNRAS, 432, 2433
Hilbert S., Hartlap J., White S. D. M., Schneider P., 2009, A&A, 499, 31
Hildebrandt H. et al., 2012, MNRAS, 421, 2355
Hinshaw G. et al., 2013, ApJS, 208, 19
Hirata C. M., Seljak U., 2004, Phys. Rev. D, 70, 063526
Hoekstra H., Franx M., Kuijken K., Squires G., 1998, ApJ, 504, 636
Hoekstra H., Franx M., Kuijken K., 2000, ApJ, 532, 88
Hoekstra H., Yee H. K. C., Gladders M. D., 2004, ApJ, 606, 67
Hoekstra H. et al., 2006, ApJ, 647, 116
Hoekstra H., Herbonnet R., Muzzin A., Babul A., Mahdavi A., Viola M., Cacciato M., 2015, MNRAS, 449, 685
Holmberg E., 1969, Ark. Astron., 5, 305
Howell P. J., Brainerd T. G., 2010, MNRAS, 407, 891
Hudson M. J. et al., 2015, MNRAS, 447, 298
Huff E. M., Eifler T., Hirata C. M., Mandelbaum R., Schlegel D., Seljak U., 2014, MNRAS, 440, 1322
Ibata R., Lewis G. F., Irwin M., Totten E., Quinn T., 2001, ApJ, 551, 294
Ilbert O. et al., 2006, A&A, 457, 841
Jing Y. P., Suto Y., 2002, ApJ, 574, 538
Joachimi B., Mandelbaum R., Abdalla F. B., Bridle S. L., 2011, A&A, 527, A26
Joachimi B., Semboloni E., Bett P. E., Hartlap J., Hilbert S., Hoekstra H., Schneider P., Schrabback T., 2013a, MNRAS, 431, 477 (J13a)
Joachimi B., Semboloni E., Hilbert S., Bett P. E., Hartlap J., Hoekstra H., Schneider P., 2013b, MNRAS, 436, 819 (J13b)
Kacprzak T., Zuntz J., Rowe B., Bridle S., Refregier A., Amara A., Voigt L., Hirsch M., 2012, MNRAS, 427, 2711
Kaiser N., Squires G., 1993, ApJ, 404, 441
Kaiser N., Squires G., Broadhurst T., 1995, ApJ, 449, 460
Kaiser N. et al., 2010, in Stepp L. M., Gilmozzi R., Hall H. J., eds, Proc. SPIE Conf. Ser. Vol. 7733, Ground-based and Airborne Telescopes III. SPIE, Bellingham, p. 77330E
Kettula K. et al., 2015, MNRAS, 451, 1460
Kilbinger M. et al., 2009, A&A, 497, 677
Kilbinger M. et al., 2013, MNRAS, 430, 2200
Kim H.-S., Baugh C. M., Cole S., Frenk C. S., Benson A. J., 2009, MNRAS, 400, 1527
Kitching T. D., Miller L., Heymans C. E., van Waerbeke L., Heavens A. F., 2008, MNRAS, 390, 149
Kitching T. D. et al., 2014, MNRAS, 442, 1326
Knebe A., Libeskind N. I., Knollmann S. R., Yepes G., Gottlöber S., Hoffman Y., 2010, MNRAS, 405, 1119
Kuhlen M., Diemand J., Madau P., 2007, ApJ, 671, 1135
Laigle C. et al., 2015, MNRAS, 446, 2744
Laureijs R. et al., 2011, preprint (arXiv:1110.3193)
Leauthaud A. et al., 2012, ApJ, 744, 159
Li C., Jing Y. P., Faltenbacher A., Wang J., 2013, ApJ, 770, L12
Libeskind N. I., Frenk C. S., Cole S., Helly J. C., Jenkins A., Navarro J. F., Power C., 2005, MNRAS, 363, 146
Limousin M., Morandi A., Sereno M., Meneghetti M., Ettori S., Bartelmann M., Verdugo T., 2013, Space Sci. Rev., 177, 155
LSST Science Collaboration et al., 2009, preprint (arXiv:0912.0201)
Ludlow A. D., Navarro J. F., Angulo R. E., Boylan-Kolchin M., Springel V., Frenk C., White S. D. M., 2014, MNRAS, 441, 378
Luppino G. A., Kaiser N., 1997, ApJ, 475, 20
Lux H., Read J. I., Lake G., Johnston K. V., 2012, MNRAS, 424, L16
Mandelbaum R., Hirata C. M., Ishak M., Seljak U., Brinkmann J., 2006a, MNRAS, 367, 611
Mandelbaum R., Seljak U., Kauffmann G., Hirata C. M., Brinkmann J., 2006b, MNRAS, 368, 715
Mandelbaum R., Hirata C. M., Broderick T., Seljak U., Brinkmann J., 2006c, MNRAS, 370, 1008 (M06)
Mandelbaum R. et al., 2011, MNRAS, 410, 844
Massey R. et al., 2007, MNRAS, 376, 13
Melchior P., Viola M., 2012, MNRAS, 424, 2757
Metz M., Kroupa P., Jerjen H., 2007, MNRAS, 374, 1125
Milgrom M., 1983, ApJ, 270, 365
Milgrom M., 2001, MNRAS, 326, 1261
Miller L., Kitching T. D., Heymans C., Heavens A. F., van Waerbeke L., 2007, MNRAS, 382, 315
Miller L. et al., 2013, MNRAS, 429, 2858
Miyazaki S. et al., 2012, in McLean I. S., Ramsay S. K., Takami H., eds, Proc. SPIE Conf. Ser. Vol. 8446, Ground-based and Airborne Instrumentation for Astronomy IV. SPIE, Bellingham, p. 84460Z
Moffat J. W., 2006, J. Cosmol. Astropart. Phys., 3, 4
Moffat J. W., Toth V. T., 2009, MNRAS, 397, 1885
Mortlock D. J., Turner E. L., 2001, MNRAS, 327, 557
Napolitano N. R. et al., 2011, MNRAS, 411, 2035
Natarajan P., Refregier A., 2000, ApJ, 538, L113
Navarro J. F., Frenk C. S., White S. D. M., 1996, ApJ, 462, 563
Navarro J. F., Frenk C. S., White S. D. M., 1997, ApJ, 490, 493
Nierenberg A. M., Auger M. W., Treu T., Marshall P. J., Fassnacht C. D., 2011, ApJ, 731, 44
Novak G. S., Cox T. J., Primack J. R., Jonsson P., Dekel A., 2006, ApJ, 646, L9
O'Brien J. C., Freeman K. C., van der Kruit P. C., 2010, A&A, 515, A63
Oguri M., Takada M., Okabe N., Smith G. P., 2010, MNRAS, 405, 2215
Oguri M., Bayliss M. B., Dahle H., Sharon K., Gladders M. D., Natarajan P., Hennawi J. F., Koester B. P., 2012, MNRAS, 420, 3213
Okamoto T., Eke V. R., Frenk C. S., Jenkins A., 2005, MNRAS, 363, 1299
Okumura T., Jing Y. P., Li C., 2009, ApJ, 694, 214
Olling R. P., Merrifield M. R., 2000, MNRAS, 311, 361
Parker L. C., Hoekstra H., Hudson M. J., van Waerbeke L., Mellier Y., 2007, ApJ, 669, 21
Parry O. H., Eke V. R., Frenk C. S., 2009, MNRAS, 396, 1972
Peng C. Y., Ho L. C., Impey C. D., Rix H.-W., 2002, AJ, 124, 266
Planck Collaboration et al. XIII, 2015, A&A, preprint (arXiv:1502.01589)
Refregier A., Kacprzak T., Amara A., Bridle S., Rowe B., 2012, MNRAS, 425, 1951
Saghiha H., Hilbert S., Schneider P., Simon P., 2012, A&A, 547, A77
Schneider P., 2006, in Meylan G., Jetzer P., North P., eds, Gravitational Lensing: Strong, Weak & Micro. Springer-Verlag, Berlin, p. 269
Schneider P., Watts P., 2005, A&A, 432, 783
Schneider M. D., Frenk C. S., Cole S., 2012, J. Cosmol. Astropart. Phys., 5, 30
Schrabback T. et al., 2010, A&A, 516, A63
Sellwood J. A., Kosowsky A., 2002, in Da Costa G. S., Sadler E. M., Jerjen H., eds, ASP Conf. Ser. Vol. 273, The Dynamics, Structure & History of Galaxies: A Workshop in Honour of Professor Ken Freeman. Astron. Soc. Pac., San Francisco, p. 243
Sifón C., Hoekstra H., Cacciato M., Viola M., Köhlinger F., van der Burg R. F. J., Sand D. J., Graham M. L., 2015, A&A, 575, A48
Simon P., Schneider P., Kübler D., 2012, A&A, 548, A102
Simon P. et al., 2015, MNRAS, 449, 1505
Singh S., Mandelbaum R., More S., 2015, MNRAS, 450, 2195
Springel V. et al., 2005, Nature, 435, 629

Suyu S. H. et al., 2012, ApJ, 750, 10
Tenneti A., Mandelbaum R., Di Matteo T., Feng Y., Khandai N., 2014, MNRAS, 441, 470
The Dark Energy Survey Collaboration 2005, preprint (astro-ph/0510346)
van de Ven G., Falcón-Barroso J., McDermid R. M., Cappellari M., Miller B. W., de Zeeuw P. T., 2010, ApJ, 719, 1481
van Uitert E., Hoekstra H., Velander M., Gilbank D. G., Gladders M. D., Yee H. K. C., 2011, A&A, 534, A14
van Uitert E., Hoekstra H., Schrabback T., Gilbank D. G., Gladders M. D., Yee H. K. C., 2012, A&A, 545, A71
Velander M. et al., 2014, MNRAS, 437, 2111
Velliscig M. et al., 2015, MNRAS, 453, 721
Vera-Ciro C., Helmi A., 2013, ApJ, 773, L4
Vera-Ciro C. A., Sales L. V., Helmi A., Frenk C. S., Navarro J. F., Springel V., Vogelsberger M., White S. D. M., 2011, MNRAS, 416, 1377
Viola M., Kitching T. D., Joachimi B., 2014, MNRAS, 439, 1909
von der Linden A. et al., 2014, MNRAS, 439, 2
Wang Y. O., Lin W. P., Kang X., Dutton A., Yu Y., Macciò A. V., 2014, ApJ, 786, 8
Wright C. O., Brainerd T. G., 2000, ApJ, 534, 34
Yang X., van den Bosch F. C., Mo H. J., Mao S., Kang X., Weinmann S. M., Guo Y., Jing Y. P., 2006, MNRAS, 369, 1293
Zhang Y., Yang X., Wang H., Wang L., Mo H. J., van den Bosch F. C., 2013, ApJ, 779, 160

APPENDIX A: TESTS WITH THE 'CLONE' IMAGE SIMULATION

Miller et al. (2013) and Heymans et al. (2012) present detailed tests of the *lens*fit shape estimation algorithm for cosmic shear measurements. As the required level of systematics control is less demanding for galaxy–galaxy lensing studies than for cosmic shear, we do not present general shape measurement tests again in the current work. However, what has not been tested before in detail, is the recovery of galaxy shapes in the presence of a nearby bright lens galaxy, whose light might affect the shape measurement process for sources at small angular separations (e.g. smaller than the 9 arcsec

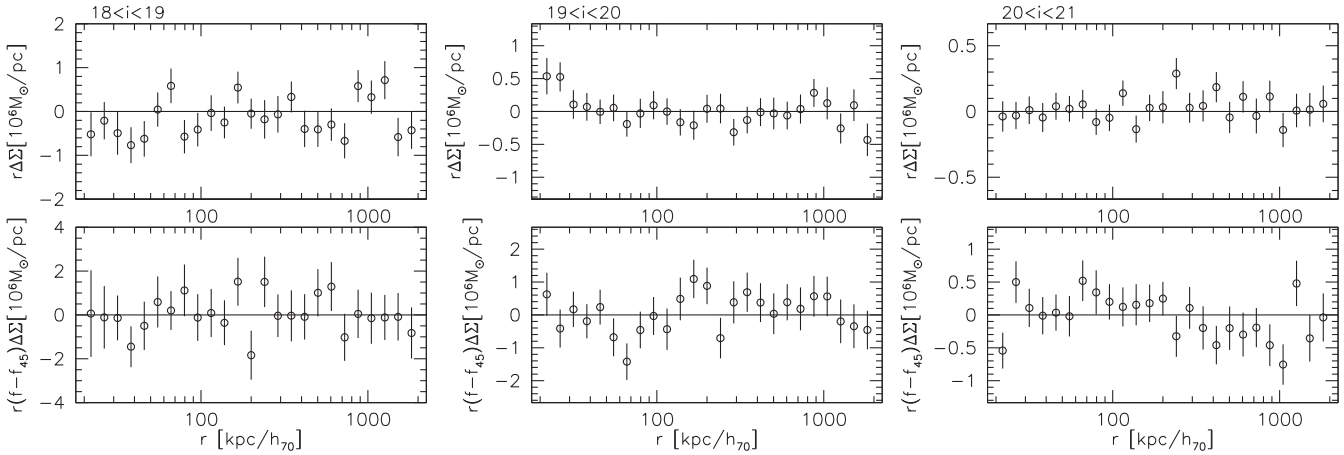

Figure A1. Test for a potential systematic contamination of the small-scale halo shape signal originating from *lens*fit shape measurements in the presence of a nearby bright galaxy (lens): we employ *lens*fit shape measurements of the 'Clone' image simulation, which uses actual galaxy positions and magnitudes from CFHTLenS as input but no galaxy–galaxy lensing signal. To optimize the sensitivity of the test, all bright galaxies in the indicated i-band magnitude intervals with *lens*fit shape estimates in the CFHTLenS data were used as lens sample (left: $18 < i < 19$, middle: $19 < i < 20$, right: $20 < i < 21$), irrespectively of their assigned CFHTLenS redshift (we assume our central lens redshift $z = 0.4$ for the computation of angular diameter distances). The top (bottom) panels show the isotropic (anisotropic) shear signal, where both have been scaled by r for better readability of the plot.

postage-stamp size).[14] To test if this could be a concern for our study, we investigate *lens*fit shape measurements of the 'Clone' image simulations (Miller et al. 2013). These simulations contain simulated galaxy images with the positions and magnitudes from CFHTLenS and cosmological shear from an *N*-body simulation (Harnois-Déraps, Vafaei & Van Waerbeke 2012) as input, but no galaxy–galaxy lensing signal. Hence, any detected galaxy–galaxy lensing signal would indicate a spurious effect introduced by the measurement process.

The result of this test is shown in Fig. A1. Here, we split the 'lenses' into magnitude bins and have subtracted the intrinsic ellipticity and cosmological shear from the measured ellipticities to maximize the S/N of the test and achieve statistical error bars which are significantly smaller than for the actual survey.[15] Given the lack of a clear signal at small scales, and the significantly smaller uncertainties compared to the CFHTLenS constraints, we conclude that the light of nearby bright lenses does not appear to introduce significant spurious signal for our halo shape analysis.

[14] For example, a circular source might appear slightly elliptical due to contamination by light from the nearby lens, where the net ellipticity would point towards the lens, thus generating spurious signal with $\Delta\Sigma < 0$. This effect would likely be stronger along the direction of the lens major axis, and could thus also generate $f\Delta\Sigma < 0$.

[15] In contrast to Miller et al. (2013), we do not make use of rotated galaxy pairs in the simulations, which are often used to partially cancel shape noise from the intrinsic source ellipticities. This combination is not useful for our test, as also the nearby 'lenses' will be rotated, therefore leading to different lens-light contributions in the rotated source galaxy pairs.

This paper has been typeset from a TEX/LATEX file prepared by the author.